Chemical Science

Accepted Manuscript

This article can be cited before page numbers have been issued, to do this please use: W. Li, X. Huang, L. Xu, X. Lu and Z. Li, *Chem. Sci.*, 2026, DOI: 10.1039/D6SC02823C.

ROYAL SOCIETY OF CHEMISTRY

rsc.li/chemical-science

View Article Online
DOI: 10.1039/D6SC02823C

REVIEW

The Electron Buffer Effect for Advanced Electrocatalysis

Weimo Li,*[a,c,d] Xiwen Huang,[d] Lin Xu,[c] Xiaofeng Lu*[b] and Zhengquan Li*[a,c,d]

Received 00th January 20xx,
Accepted 00th January 20xx

DOI: 10.1039/x0xx00000x

The electronic structure of catalysts often undergoes irreversible transformation during electrocatalysis under applied potential, significantly impacting their activity and stability. Recent studies have revealed the critical role of the electron buffer effect in enhancing electrocatalytic performance. Conceptually analogous to a pH buffer, this effect involves the dynamic regulation of electron density at active sites through reversible electron transfer with a functional support. It helps stabilize the optimal valence states of active sites, mitigates over-oxidation or over-reduction, and optimizes the adsorption/desorption behavior of key reaction intermediates. These insights underscore the need for a deeper atomic-level understanding of dynamic electronic structure design. This review systematically elaborates the fundamental mechanisms and distinctive features of the electron buffer effect, categorizes the relevant buffer materials into metal-based and nonmetal-based systems, and highlights their crucial roles in key electrocatalytic reactions. Finally, current challenges and future prospects concerning the precise manipulation and characterization of electron buffer effects are discussed, providing guidance for the rational design of advanced materials in highly efficient electrocatalysis.

1. Introduction

The global energy landscape remains heavily dependent on the traditional fossil fuels, which drive the socioeconomic development.[1,2] However, this persistent reliance intensifies the dual crisis of energy shortage and environmental pollution, underscoring the urgent need to accelerate the global energy transition and achieve carbon neutrality.[3–5] In this context, the utilization of renewable electricity to drive chemical transformation reactions has emerged as a cutting-edge and pivotal research direction in chemistry and materials science.[6] Electrocatalysis holds immense promise for storing intermittent renewable energy (e.g., solar and wind) in the form of chemical bonds, and converting it into value-added fuels and chemicals.[7,8] Currently, key techniques including water splitting for hydrogen production, fuel cells, CO_2 conversion, and ammonia production are garnering widespread interest, which involve critical electrocatalytic reactions such as hydrogen/oxygen evolution reaction (HER/OER), oxygen reduction reaction (ORR), CO_2 reduction reaction (CO_2RR), and nitrogen/nitrate reduction reaction (NRR/NO_3RR).[9–13] Nevertheless, the widespread implementation of these electrocatalytic processes is still hindered by inherent challenges, including sluggish reaction kinetics, high overpotential, and limited energy conversion efficiency.[14,15] Consequently, the fundamental understanding of catalytic mechanisms, coupled with the rational design of highly efficient electrocatalysts that exhibit superior activity and stability, is essential to propel these electrochemical reactions towards large-scale practical application.

Early research in electrocatalysis predominantly focused on modulating the geometric structure of catalysts, such as particle size, morphology, and exposed specific surface area.[16,17] However, these strategies faced inherent limitations, as the intrinsic activity of an electrocatalyst is governed not merely by the number of active sites, but more critically by its electronic structure. Specifically, the electronic density of states near the Fermi level, particularly the *d*-band center in transition metals, determines the degree of orbital overlap between reactant molecules and the catalyst, thereby precisely regulating the adsorption strength of reaction intermediates. In 1978, Tauster et al. reported a pronounced suppression of H_2 and CO chemisorption on Pt/TiO_2, following high-temperature reduction (HTR), leading to the pioneering concept of the strong metal-support interaction (SMSI) mechanism.[18] The efficient electron transfer from support to metal was found to fundamentally alter the electronic density of the metal surface. Since then, SMSI effect has been observed across various supported catalysts induced by diverse methods (e.g., reduction, oxidation, photo-treatment).[19] This discovery provided profound insight into how “inert” support governs the electronic structure and adsorption behavior of a metal catalyst through electronic interaction effect. Nonetheless, according to the Sabatier principle, an ideal catalyst should exhibit moderate adsorption strength toward reaction intermediates to facilitate their rapid generation and facile desorption. Furthermore, under harsh electrocatalytic conditions, active sites are susceptible to irreversible oxidation or reduction, leading to rapid catalyst deactivation. Hence, developing effective strategies to precisely regulate and maintain the optimal electronic structure of active sites has become a paramount objective in catalyst design.

[a] College of Physics and Electronic Information Engineering, Department of Materials Science and Engineering, Zhejiang Normal University, Jinhua, Zhejiang 321004, P. R. China. E-mails: liweimo@zjnu.edu.cn; zqli@zjnu.edu.cn
[b] Alan G. MacDiarmid Institute, College of Chemistry, Jilin University, 2699 Qianjin Street, Changchun 130012, P. R. China. E-mail: xflu@jlu.edu.cn
[c] Zhejiang Institute of Photoelectronic, Zhejiang Normal University, Jinhua, Zhejiang 321004, P. R. China.
[d] Key Laboratory of the Ministry of Education for Advanced Catalysis Materials, Zhejiang Normal University, Jinhua, Zhejiang 321004, P.R. China.

With the development of nanotechnology and carbon-based materials, the SMSI-like effect has been observed in some novel carbon structures, such as sulfur-doped carbon and graphene.[20,21] Inspired by the concept of a buffer solution resisting pH changes, the more advanced electron buffer effect was proposed to describe the reversible electron exchange between metal nanoparticles and highly conductive carbon supports. In this mechanism, the conductive carbon support serves as an "electron reservoir", dynamically donating or accepting electrons in response to variations in external potential or reaction conditions , which has been recently validated in the thermocatalytic processes for ethylene glycol and ammonia synthesis.[22,23] Owing to the delocalized π electron system, carbon supports can rapidly respond to environmental changes and promptly modulate the electronic structure of metal centers.[24] By dynamically mitigating the over-oxidation or over-reduction of the metal sites, the induced electron buffer effect effectively stabilizes the optimal valence state of active sites, leading to favorable intermediate adsorption and enhanced catalytic performance.[25] Currently, this concept has expanded beyond carbon materials to other functional compounds (e.g., CeO_2),[26] and from heterostructures to atomic-level doped architectures.[27,28] In view of these superior features, inducing electron buffer effect to precisely regulate the electronic structure of the active sites has emerged as the key strategy for improving the electrocatalytic performance. However, the efficacy of this effect is highly dependent on the integrity of interfaces between components, which may become unstable under severe electrochemical environment due to elemental dissolution, phase transformation, and undesirable surface reconstruction. Therefore, a timely review that systematically outlines the mechanisms, applications and challenges of electron buffer effect in electrocatalysis is urgently needed.

In this review, we highlight the fundamental mechanisms and origins of the electron buffer effect and establish its integral connection to electrocatalytic processes (Fig. 1). We systematically classify the materials capable of inducing electron buffer effect into two groups, including metal-based components and nonmetal-based components. More importantly, this review categorizes and elaborates on the pivotal role of the electron buffer effect across major important electrocatalytic reactions (e.g., OER, HER, ORR, CO_2RR, NRR, and NO_3RR), highlighting its contribution to boosting catalytic activity and stability by optimizing the adsorption/desorption behavior of key intermediates and stabilizing the valence states of active sites. Finally, we discuss the prevailing challenges and future prospects in the precise manipulation and real-time characterization of electron buffer effects, aiming to inspire the rational design of high-performance electrocatalysts.

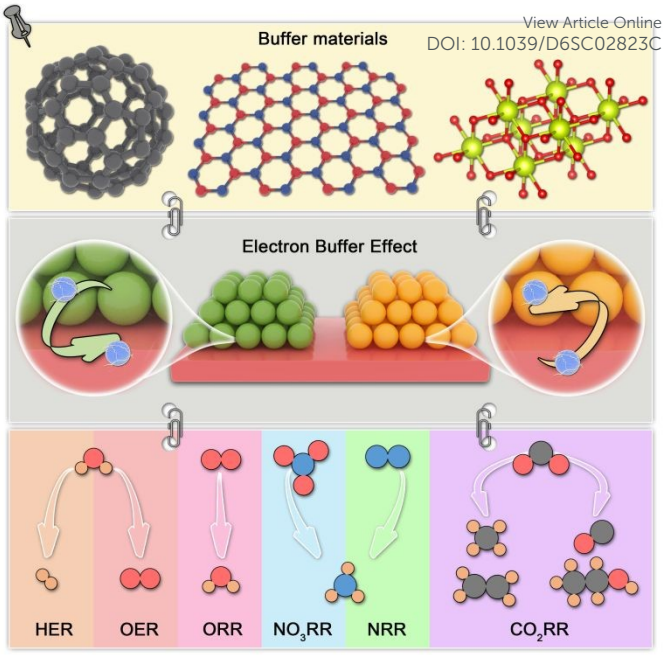

Fig. 1 Schematic illustration of electron buffer effect for electrocatalysis.

2. Fundamentals of Electron Buffer Effect in Electrocatalysis

The rational design of advanced electrocatalysts necessitates a profound understanding of interfacial electronic effects, among which the electron buffer effect has emerged as a pivotal strategy for enhancing catalytic performance. Distinct from conventional strategies that focus solely on the intrinsic properties of active sites, this effect enables dynamic regulation of the electronic structure, allowing real-time adaptation to demanding electrochemical environment. Hence, a concise analysis of the mechanism and unique features of the electron buffer effect serves as starting point for this review (Fig. 2).

2.1. Mechanism

The core mechanism of the electron buffer effect lies in the ability of material with specific electron structure to function as a dynamic "electron reservoir", reversibly injecting or extracting electrons into adjacent active sites in response to fluctuations in external potential or reaction microenvironment. Physically, this is not a static electron distribution. This behavior originates from the electronic interactions in a built-in electron channel at the interface between active sites and buffer component. A promising buffer component can undergo repeated redox cycles (filling/emptying of its frontier orbitals or bands) with minimal structural degradation or significant shift in its intrinsic buffering potential, thereby sustaining its function. For instance, under highly oxidation environments, the active sites are prone to over-oxidation, forming high-valence soluble species, such as RuO_2 in acidic OER process.[29] In such cases, the buffer component functions as the electron donor, rapidly supplying electrons to stabilize the oxidation states of metal sites and thereby preserving stability of catalyst. Conversely, in many cathodic reactions, the active sites may become over-reduced, which diminishes their capacity for reactant adsorption and activation. Here, the electron

buffer effect can promptly snatch excess electrons from the active sites, maintaining a moderately electron-deficient state that favors intermediate adsorption.[30] Therefore, the electron buffer effect holds great promise for advancing electrocatalytic systems.

2.2. Multifunctional Roles in Catalysis

Compared to traditional single-component catalysts or synergistic effect, the electron buffer effect is not a static electronic modification, but a dynamic and continuous equilibrium process capable of real-time adaptation to the reaction environment. Moreover, this effect operates spontaneously during electrocatalytic process, preventing the active sites from deviating from their optimal electronic state, rather than repairing them after deactivation, thereby fundamentally enhancing catalytic stability. Beyond regulating the valence state of active sites for stability optimization, the electron buffer effect also exhibits several other distinctive capabilities. First, by finely tuning the electron density of active sites, it induces shifts in the d-band center position, which effectively modulates the adsorption energy of key intermediates and significantly reduces the overpotential.[31] Second, the built-in electron channels established by this effect facilitate rapid electron shuttling across surface and interface of catalyst, lowering the charge transfer resistance and accelerating reaction kinetics.[26] Third, in multiple-step reactions involving multiple intermediates, the electron buffer effect can disrupt linear scaling relationships among the key intermediates by altering the adsorption behavior of the key intermediates.[32] Therefore, the deliberate incorporation of electron buffer effect opens a novel avenue for designing catalytic materials that surpass the performance limitations of conventional catalysts.

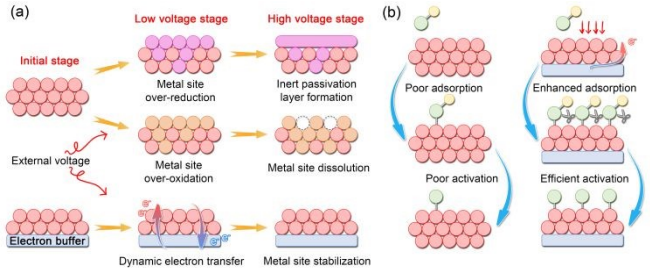

Fig. 2 Schematic illustration of electron buffer effect toward (a) modulation of valence state and (b) intermediate adsorption behaviors.

3. *In Situ* Characterization Techniques

In situ characterization techniques are indispensable for unravelling the dynamic evolution of catalysts under operating conditions, which allows real-time monitoring of changes in the valence state, local coordination environment, and reaction intermediates, providing direct evidence for electron buffer effect. In this section, we summarize several *in situ* characteristic techniques, including *in situ* X ray absorption near-edge spectroscopy/extended X-ray adsorption fine structure (XANES/EXAFS), *in situ* X-ray photoelectron spectroscopy (XPS), *in situ* Fourier-transform infrared spectroscopy (FTIR), and *in situ* Raman.

3.1. *In situ* XANES and EXAFS

The *in situ* XANES and EXAFS can monitor the dynamic valence state and coordination structure changes of both active sites and buffer components.[28,32,33] Peng et al. developed an inter-doped tungsten–ruthenium oxide [(Ru–W)O_x] catalyst and used *in situ* XANES and EXAFS techniques to monitor the dynamic changes in Ru oxidation states under operating conditions.[33] For (Ru–W)O_x, starting from the open-circuit voltage (OCV) to 1.4 V vs. RHE, the average Ru valence state slightly decreased from +3.7 to +3.5, which corresponds to a pre-catalytic redox process (Fig. 3a). As the potential rose from 1.4 V to 1.6 V vs. RHE, the Ru valence increased from +3.5 to +4.1, indicating the formation of higher-valent Ru sites that are active for OER. Remarkably, when the potential exceeded 1.8 V vs. RHE, the Ru oxidation state decreased again from +4.1 back to approximately +3.7. This reversible decrease demonstrated that the high-valent W species donate electrons back to the Ru sites and prevent their over-oxidation to soluble RuO_4^{2-} species. In contrast, the RuO_x catalyst showed a continuous and irreversible increase in Ru valence state with increasing potential, leading to structural degradation and Ru dissolution (Fig. 3a). Besides, *in situ* EXAFS analysis indicated that (Ru–W)O_x possessed a minor increase in Ru–O coordination number (CN) while RuO_x exhibits a significant decrease in CN, which is attributed to the structural damage (Fig. 3b). Hence, the (Ru–W)O_x enables a reversible valence oscillation of Ru sites and stabilizes the Ru–O coordination structure, thereby enhancing its stability.

3.2 *In situ* XPS

The *in situ* XPS can also quantitatively track the valence state of active site under operating conditions.[26,34,35] For example, Guo et al. fabricated an iridium–cerium substitution solid solution oxide (Ir–Ce SSO) for efficient OER and used XPS to investigate the valence state change of Ir species in Ir–Ce SSO.[35] After operating at different potentials, the XPS spectra revealed that the amount of Ir^{3+} species in Ir–Ce SSO decreases slowly, just from 51.8% to 35.5% (Fig. 3c). This result suggested that the CeO_2 with electron buffer effect effectively inhibits the over-oxidation and dissolution of Ir from in Ir–Ce SSO. Hence, the Ir–Ce SSO showed the great stability in PEMWE device with 100 h at 500 mA cm^{-2}. Besides, the binding energy shifts of active site and buffer component can be also observed with the change of applied potential, which can directly reflect the electron buffer effect during electrocatalytic process. Therefore, *in situ* XPS can provide intuitive evidence for dynamic changes in charge state through the changes of binding energies and peak area.

3.3. *In situ* FTIR

By probing the vibrational adsorption modes of chemical bonds on the catalyst surface, *in situ* FTIR allows real-time determination of reaction intermediate and their adsorption configurations, which can be used to analyze the impact of electron buffer effect on the catalytic process and mechanism.[36,37] Liu et al. synthesized a Ru/Ta_2O_5 catalyst with abundant 5d electron buffering interface.[36] The anchoring of Ru on the surface of Ta_2O_5 modulated the electron cloud density around Ru sites via Ta 5d electrons, optimizing the reaction pathway from adsorbate evolution mechanism (AEM) to oxide path mechanism (OPM), which was confirmed by *in situ* FTIR technique. The RuO_2 exhibited a peak near 1120 cm^{-1} under high potentials, attributed to *OOH species, suggesting that it proceeds via the AEM pathway at high potentials (Fig. 3d). In contrast, for Ru/Ta_2O_5, distinct absorption peaks at 1033 cm^{-1} and 1067 cm^{-1} appeared at potentials above 1.3 V vs. RHE, which are assigned to adsorbed *O–O* and *O–O intermediates, indicating that the

catalyst follows the OPM pathway where direct O–O coupling releases O_2 without forming *OOH intermediates (Fig. 3e). Hence, *in situ* FTIR can effectively reflect the influence of electron buffer effect on regulating the reaction intermediates.

3.4. *In situ* Raman

In situ Raman can not only detect the reaction intermediates but also reflect the structural transformation during electrocatalytic process.[30,38,39] Fu et al. prepared an atomically dispersed Ce on CoO (P-Ce SAs@CoO) catalyst for OER.[38] As shown in *in situ* Raman spectra of P-Ce SAs@CoO and CoO, three characteristic Co–O vibrational modes of the CoO phase at 482 cm^{-1}, 521 cm^{-1}, and 690 cm^{-1}, along with a broad peak between 580 cm^{-1} and 620 cm^{-1} assigned to Co–OH species formed by OH^- adsorption at low potential. As the applied potential increased, CoO showed a rapid attenuation of the Co–O peak intensities beyond 0.45 V vs. Ag/AgCl, suggesting the surface reconstruction, lattice oxygen evolution, and dissolution-redeposition processes of the catalysts during OER (Fig. 3f). However, P-Ce SAs@CoO preserved the Co–O vibrational signals even at high potentials, indicating that the introduction of Ce SAs significantly strengthens the Co–O bond and suppresses its breakage during OER (Fig. 3g). Normalized intensity analysis of the A_{1g} peak (690 cm^{-1}) further confirmed that the Ce–O–Co unit site remains stable under harsh oxidative conditions. The *in situ* Raman results revealed that Ce acts as an electronic protector that prevents the structural degradation of CoO, thereby enhancing both activity and stability for the oxygen evolution reaction.

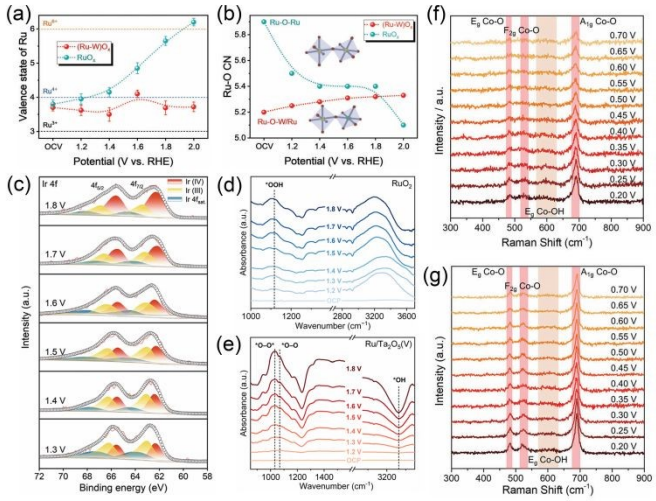

Fig. 3 (a) The valence states and (b) the Ru–O coordination numbers of RuO_x and $(Ru–W)O_x$ at different potentials. Reproduced with permission.[33] Copyright 2023, Wiley-VCH. (c) XPS spectra of Ir–Ce SSO after operating at different potentials. Reproduced with permission.[35] Copyright 2024, Wiley-VCH. *In situ* FTIR spectra of (d) RuO_2 and (e) Ru/Ta_2O_5. Reproduced with permission.[36] Copyright 2025, Royal Society of Chemistry. *In situ* Raman spectra of (f) CoO and (g) P-Ce SAs@CoO. Reproduced with permission.[38] Copyright 2023, Wiley-VCH.

4. Material Platforms for Electron Buffering

As emphasized earlier, the realization of the electron buffer effect hinges critically on the inherent electronic properties of the buffer component. A systematic understanding of such materials is vital for the rational design of high-performance electrocatalysts. This section comprehensively introduces materials capable of inducing the electron buffer effect, which are primarily categorized into two groups including metal-based and nonmetal-based systems.

4.1. Metal-based Components

The key feature of these metal-based buffer components is the reversible multi-electron redox capability of their metal centers, which allows them to function as localized electron exchange reservoirs. As the most representative metal-based material, CeO_2 exhibits the significant electron buffering capability owing to the Ce^{3+}/Ce^{4+} redox couple and the formation/annihilation of oxygen vacancies within its stable fluorite crystal structure.[26,35,40–43] The shielding effect of 5s/5p orbitals, progressive filling of 4f orbital, and the presence of abundant electronic energy levels endow Ce with a highly adaptable pathway for electronic structure optimization. For instance, Wang et al. developed a scalable strategy to achieve dynamic electron backflow across heterogeneous interfaces by constructing CeO_2/Fe–$Co(OH)_2$ heterojunction.[26] Driven by the built-in electric field at the interfaces between CeO_2 and $Co(OH)_2$, the resulting high-valence $Co^{\delta+}$ species synergistically activate lattice oxygen with high-spin Fe^{3+}, significantly enhancing catalytic activity (Fig. 4a). Moreover, the higher work function of Fe–CoO_2 compared with CeO_2 provides the driving force for the electron backflow from CeO_2 to Fe–CoO_2, thereby suppressing the over-oxidation of Co and improving structural stability (Fig. 4b). Besides, the d-band center of CeO_2/Fe–$Co(OH)_2$ lied between those of Fe–$Co(OH)_2$ and CeO_2/$Co(OH)_2$, indicating the optimized adsorption strength for intermediates. The CeO_2/Fe–$Co(OH)_2$ exhibited the overpotential of 189 mV at 10 mA cm^{-2} and maintained 800 h at 1000 mA cm^{-2}, which outperformed Fe–$Co(OH)_2$ (220 mV at 10 mA cm^{-2} and 100 h at 1000 mA cm^{-2}). This reversible electron shuttling between $Co^{2+} \rightarrow Ce^{3+/4+}$ and $Ce^{3+/4+} \rightarrow Co^{3+/4+}$, which is induced by the electron buffer effect of CeO_2, dynamically modulates the valence state of Co active sites, thereby enhancing both electrocatalytic activity and operational stability. Beyond Ce-based systems, other variable-valence metals characterized by weak electron affinities and strong ionization tendencies can also serve as the effective electron buffer components, which mitigate the localized charge imbalance and polarization to achieve a more uniform electron density distribution.[27,28,36] Li et al. introduced Cr into intermetallic PtFe alloy nanoparticle to modulate the electronic structure of Pt shells.[28] In $L1_0$-PtFe/C system, partial oxidation of Pt shell increases surface charge density, inducing electrostatic repulsion and lattice expansion (Fig. 4c). Encouragingly, the incorporation of Cr as an electron buffer with electron-donating ability effectively suppresses the surface polarization of Pt shells by relieving the increase of the valence state and the tensile strain under increasing potential (Fig. 4d and e). The $L1_0$-Cr-PtFe/C showed a moderate d-band center position (–2.487 eV) compared to that of $L1_0$-PtFe/C (–2.541 eV) and pure Pt (–2.382 eV), indicating the optimized adsorption of surface oxygen species. This mechanism significantly enhances the electrocatalytic activity and simultaneously inhibits the dissolution of both Pt and Fe. $L1_0$-Cr-PtFe/C possessed the half-wave potential of 0.952 V and maintained 30000 ADT cycles with 2.9% degradation, which are superior than those of $L1_0$-PtFe/C (almost 0.92 V and 30000 ADT cycles with 20.2% degradation). Therefore, in designing advanced electrocatalysts with

View Article Online
DOI: 10.1039/D6SC02837C

electron buffer functionality, the strategic utilization of the multi-valence metal-based buffer components, coupled with precise electron density modulation, offers a powerful approach to simultaneously boost electrocatalytic activity and long-term stability.

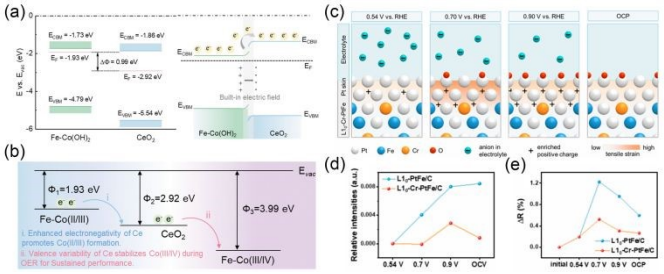

Fig. 4 (a) Schematic diagram of band structures for Fe–Co(OH)$_2$, CeO$_2$, and CeO$_2$/Fe–Co(OH)$_2$. (b) The proposed work functions of CeO$_2$/Fe–Co(OH)$_2$ during OER. Reproduced with permission.[26] Copyright 2025, Royal Society of Chemistry. (c) Schematic diagram of electrochemical processes on L1$_0$-Cr-PtFe/C under different potentials. *In situ* potential-dependent relative (d) white-line intensity and (e) radial distances of L1$_0$-Cr-PtFe/C and L1$_0$-PtFe/C. Reproduced with permission.[28] Copyright 2024, American Chemical Society.

4.2. Nonmetal-based Components

Nonmetal-based materials offer a distinct and powerful platform for electron buffering, operating not through valence state changes in metal cations but via defect engineering and delocalized electron systems. The spherical structure and highly delocalized three-dimensional π-electron system of fullerene (C$_{60}$) grant it high electron affinity, and its low-energy lowest unoccupied molecular orbital (LUMO) acts as a dedicated electron reservoir, enabling it to function as an electron buffer component to reversibly accept or donate electrons in response to the surrounding electronic environment.[34,44–46] Zhang et al. developed a C$_{60}$-buffered Ru-RuO$_2$ heterostructure (Ru-RuO$_2$/C$_{60\text{-}x}$), in which the Ru-based active species reversibly transition between Ru and RuO$_2$ during HER and OER.[34] When the applied potential decrease from open-circuit-potential (OCP) to –0.4 V, C$_{60\text{-}x}$ donated electrons to RuO$_2$ (Ru^{4+}), inducing the generation of more Ru^0 species (Fig. 5a and b), which is beneficial for lowering the adsorption energy barrier of *H intermediates. Conversely, during OER process, C$_{60\text{-}x}$ withdraw the electrons from Ru^0 species to facilitate the regeneration of Ru^{4+} species, thereby enhancing the OER activity (Fig. 5a and c). The Bader charge results showed that C$_{60\text{-}x}$ tended to transfer more negative charge (0.68 |e|) to the surface Ru atoms compared with carbon nanotube (0.01 |e|) and graphene (0.13 |e|), which effectively alleviating the fully oxidation of Ru to RuO$_2$ and stabilizing the desired Ru/RuO$_2$ heterostructure. This C$_{60\text{-}x}$-mediated dynamic interfacial reconstruction between Ru^0 and Ru^{4+} enables the catalyst to exhibit excellent bifunctional electrocatalytic activity for both HER and OER (Fig. 5d). Ru-RuO$_2$/C$_{60\text{-}x}$ exhibits the overpotentials of 7 and 198 mV at 10 mA cm^{-2} for HER and OER, which are lower than those of RuO$_2$ (129 and 265 mV). Furthermore, the strong intermolecular interactions among C$_{60}$ molecules facilitate the formation of thin and highly dispersible C$_{60}$ crystals. Recently, the two-dimension (2D) C$_{60}$ network assembled with covalently bonded C$_{60}$ cages within a plane has been successfully exfoliated from bulk crystals through micromechanical cleavage and intercalation-based exfoliation method.[32,47,48] Yang et al. synthesized few-layer 2D-C$_{60}$ networks using an acid etching-liquid exfoliation method, and integrated them with Ru nanoparticles to construct Ru NPs/2D-C$_{60}$.[49] The Bader charge analysis revealed that under the electron buffer effect of C$_{60}$ with an electron-withdrawing ability, Ru loses few electrons (from 0.63 |e| to 0.52 |e|), increasing the electron density of *H and *OH species (from 0.17 |e| and 0.22 |e| to 0.38 |e| and 0.41 |e|, respectively), thereby accelerating their desorption and ultimately improving the HER activity. Ru NPs/2D-C$_{60}$ exhibits the overpotential of 24 mV at 10 mA cm^{-2}, which is lower than that of Ru NPs (74 mV). Beyond pristine C$_{60}$, fullerenol (C$_{60}$(OH)$_x$) functionalized with hydroxyl groups not only offers abundant O sites to anchor metal species (e.g., Ru, Ni, and Fe) but also retains the inherent advantages of C$_{60}$, making it another effective regulator of the interfacial electronic structure in electrocatalysis.[50,51]

Apart from carbon-based materials, hexagonal boron nitride (BN) has also emerged as a promising electron buffer support for modulating the electron density of active sites. The B and N sites in BN act as electron-deficient and electron-rich centers, respectively, creating polarized B–N bond that enable flexible regulation of the electronic structure of supported catalysts.[52] However, conventional hexagonal BN is an electrical insulator with poor conductivity, which limits efficient directional electron transfer. Constructing atomically thin BN nanosheets has proven effective in facilitating rapid electron tunneling in the direction perpendicular to the exposed plane.[53] Peng et al. designed a defect-rich ultrathin BN nanosheets as the support for RuO$_2$ (RuO$_2$/BNNS).[54] In this hybrid, N sites serve as Lewis base sites that donate electron to Ru, suppressing its over-oxidation while B sites functions as Lewis acid sites that accept electrons from O, thereby stabilizing the lattice oxygen species (Fig. 5e). Hence, there is a bidirectional electron transfer between Ru and BNNS. Leveraging this mechanism, RuO$_2$/BNNS displayed remarkable activity and stability compared to traditional heterojunction catalysts. Normally, as the applied potential increases, the sluggish replenishment of surface charges leads to electron loss from surface oxygen, triggering oxygen release and structural collapse (Fig. 5f). In contrast, the local charge cycling induced by BNNS effectively maintained the electrocatalytic stability of RuO$_2$/BNNS with the slight fluctuations of Ru oxidation state around 3.92. Moreover, the polarized B sites are susceptible to the nucleophilic attacks, which facilitates the deprotonation of *OH and *OOH intermediates on Ru sites. Therefore, RuO$_2$/BNNS possessed the overpotential of 180 mV at 10 mA cm^{-2}, which is lower than that of RuO$_2$ (270 mV). In addition to structural design, introducing interstitial oxygen can also induce an electron buffer effect to regulate the electron localization behavior.[37] Guo et al. designed a CrMnFeNiPt high entropy alloy (HEA) catalyst, in which the strong oxygen affinity of Cr facilitated the incorporation of oxygen as an electron buffer with a strong electron-withdrawing ability.[37] The presence of interstitial oxygen modulated the electron density of adjacent metal atoms, reducing their d-band centers and increasing their vacancy formation energies, thereby enhancing the electrocatalytic performance. In summary, nonmetal-based electron-buffering materials represents a highly promising direction for further electrocatalyst design.

View Article Online
DOI: 10.1039/D6SC00823G

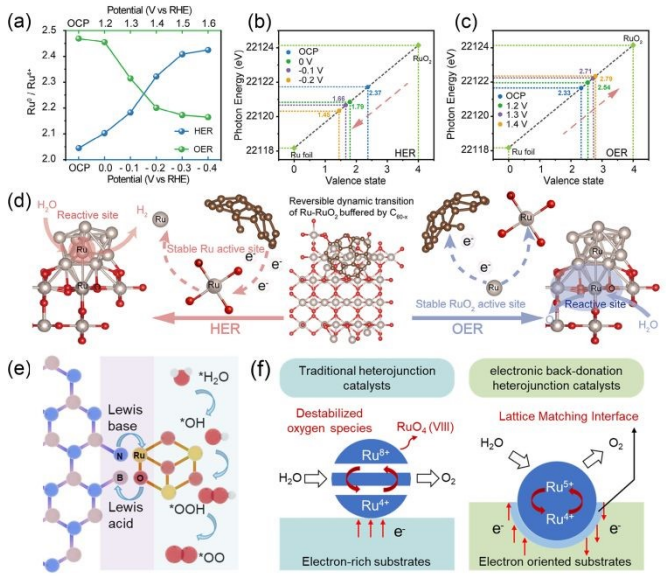

Fig. 5 (a) The ratio of Ru^0/Ru^{4+} in Ru-RuO_2/C_{60-x} against applied potential in HER and OER. Valence state of Ru in Ru-RuO_2/C_{60-x} against applied potential in (b) HER and (c) OER. (d) Schematic illustration of reversible dynamic transition of Ru-RuO_2/C_{60-x} during HER and OER. Reproduced with permission.[34] Copyright 2025, Wiley-VCH. (e) Schematic illustration of electron transport between RuO_2 and BNNS. (f) Schematic illustration of charge compensation and transition process on the different heterojunctions. Reproduced with permission.[54] Copyright 2024, Wiley-VCH.

4.3. Selection principle

Due to the different buffering mechanisms of nonmetal-based and metal-based buffer materials, their roles in electrocatalytic reaction are also different. Taking C_{60} as an example of nonmetal-based materials, its three-dimensional π-electron system enables reversible acceptance/release of multiple electrons, stabilizing the valence state of adjacent metal active centers and preventing their over-oxidation or over-reduction. The cage structure of C_{60} exhibits high thermal stability and chemical inertness, and it serves as a stable support to offer flexible integration approaches (van der Waals forces, π-π stacking, or chemical bonding) to form heterojunctions with various materials (e.g., single atoms and metal phthalocyanines). Moreover, acting as an electron transfer mediator, C_{60} can induce strong electron coupling at heterojunction interfaces, effectively reducing interfacial charge transfer resistance and accelerating reaction kinetics. However, the carbon sites in C_{60} are often catalytically inert and cannot effectively provide additional active sites. Its large molecular size may introduce steric hindrance effect that impede the adsorption of reactants at the active sites. In addition, the nonmetal-based buffer materials would suffer irreversible structural changes after exposing to an oxidative environment for a long time, which significantly compromises the efficiency of the electron buffer effect.

As for metal-based buffer materials, CeO_2, as a representative material, can accept electrons from adjacent metal–oxygen bonds, thereby effectively stabilizing the integrated metal oxides (e.g., RuO_2) against structural collapse caused by excessive delocalization of lattice oxygen electrons under high potential. This enables long-term stable operation under highly oxidizing conditions, even at large current densities. Besides, CeO_2 provides abundant oxygen vacancies that originated from the Ce^{3+}/Ce^{4+} redox transition, which not only act as active sites to promote water dissociation but also facilitate the optimization of reaction intermediate adsorption. The CeO_2 exhibits excellent structural stability, maintaining good chemical resistance in both acidic and alkaline electrolytes, along with high-temperature durability. However, CeO_2 is a wide-bandgap semiconductor with intrinsically low electronic conductivity. In electrocatalysis, this shortcoming directly restricts the electron transport rate at the bulk phase and interfaces, increases the overpotential of the electrochemical reaction, thus constitutes a major bottleneck for improving efficiency. Both nonmetal-based and metal-based buffer materials possess their advantages and disadvantages. Therefore, the selection of an electron buffer material is not fixed but should be rationally guided by the specific requirements of the catalytic reaction and the nature of the active component.

5. Applications of the Electron Buffer Effect in Various Electrocatalytic Reactions

Based on the systematically established material platforms capable of inducing the electronic buffer effect, the strategic application of this mechanism to specific electrocatalytic reactions is essential for addressing their respective bottlenecks. It is noteworthy that while the physical nature of the electronic buffer effect is universal, its operational behavior under different reaction environments exhibits significant variations. These differences stem from the distinct thermodynamic energy barrier and unique kinetic pathway inherent to each reaction. This section delves into the role of the electron buffer effect across five key electrocatalytic reactions (OER, HER, ORR, CO_2RR, and NRR/NO_3RR), focusing on how it enhances electrocatalytic activity and stability under distinct electrocatalytic conditions (Table 1).

Table 1 The electrocatalytic performance of the electrocatalysts for various reactions with/without buffer components

OER					
Catalysts	Electrolyte	η (mV)@j ($mA\ cm^{-2}$)	Tafel slope ($mV\ dec^{-1}$)	Stability (h) @j ($mA\ cm^{-2}$)	Reference
$(Ru–W)O_x$	0.5 M H_2SO_4	170@10	46.2	300@10	Adv. Mater.
RuO_x		240@10	78.3	75@10	2023, 35, 2305939
$Re_{0.06}Ru_{0.94}O_2$	0.1 M $HClO_4$	190@10	45.5	200@10	Nat. Commun.
RuO_2		258@10	50.3	20@10	2023, 14, 354

View Article Online
DOI: 10.1039/D6SC02823C

Ir NCs/C_{60}NET	0.5 M H_2SO_4	237@10	41	600@10	J. Am. Chem. Soc.
Ir NCs/graphene		259@10	50	29@10	2025, 147, 20600–20611
Ir–Ce SSO	0.5 M H_2SO_4	238@10	65.9	100@10	Adv. Funct. Mater.
Com-IrO_2		297@10	77.5	40@10	2024, 34, 2400809
Ce–Mn_2O_3	160 g L^{-1} H_2SO_4	329@10	112.3	N/A	ACS Appl. Mater. Interfaces
Mn_2O_3		364@10	138.6	N/A	2025, 17, 47047−47056
CeO_2/Fe–$Co(OH)_2$	1 M KOH	189@10	39	800@1000	Energy Environ. Sci.
Fe–$Co(OH)_2$		228@10	52.9	100@1000	2025, 18, 7188–7202
IrO_x/CeO_2	0.5 M H_2SO_4	220@10	63	300@10	Nano Energy
c-IrO_x		290@10	78	30@10	2022, 104, 107960
CeO_2/FeOOH	1 M KOH	261@10	37.12	100@1000	Energy Environ. Mater.
FeOOH		281@10	49.63	40@1000	2025, 0, e70136
Mn/Ru-NC	0.5 M H_2SO_4	180@10	46.5	80@10	Chem. Eng. J.
Ru-NC		280@10	56.1	40@10	2024, 497, 154724
Ni_3Fe LDH/$NiFe_2O_4$/Pt–Tm	1 M KOH	224@10	54.81	N/A	J. Mater. Chem. A
Ni_3Fe LDH/$NiFe_2O_4$/Pt		259@10	62.61	N/A	2024, 12, 17574–17585
Ru/Ta_2O_5	0.1 M $HClO_4$	272@10	64.5	190@10	J. Mater. Chem. A
RuO_2		303@10	100.3	10@10	2025, 13, 23998–24004
Ta-RuO_2	0.1 M $HClO_4$	201@10	55	280@10	Adv. Energy Mater.
R-RuO_2		218@10	62	100@10	2025, 15, 2403388
Ru-RuO_2/C_{60-x}	1 M KOH	194@10	113.25	200@65	Angew. Chem. Int. Ed.
RuO_2		265@10	174.93	N/A	2025, 64, e202503608
$Ru_3Cr_1Sr_x$	0.1 M $HClO_4$	214@10	40.6	300@10	Nano Lett.
C-RuO_2		270@10	52.2	50@10	2024, 24, 10899−10907
RuO_2/BNNS	0.5 M H_2SO_4	180@10	63.3	350@10	Angew. Chem. Int. Ed.
RuO_2		270@10	136.9	N/A	2024, 63, e202402018
P-Ce SAs@CoO	1 M KOH	261@10	75	30@10	Adv. Mater.
CoO		310@10	80.2	5@10	2023, 35, 2302462

HER

Catalysts	Electrolyte	η (mV)@j (mA cm^{-2})	Tafel slope (mV dec^{-1})	Stability (h) @j (mA cm^{-2})	Reference
Pt_1-Mo_L-Mo_2C	1 M KOH	12@10	17	192@80	Adv. Mater.
Pt_1-Mo_2C		47@10	34	N/A	2025, 37, 2502989
RCO/TF	1 M KOH	17@10	42	N/A	J. Mater. Chem. A
RuO_2/TF		27@10	47	N/A	2025, 13, 14964–14971
Ru-RuO_2/C_{60-x}	1 M KOH	7@10	19.2	200@250	Angew. Chem. Int. Ed.
RuO_2		129@10	63.22	N/A	2025, 64, e202503608
Ru NPs/2D-C_{60}	1 M KOH	24@10	41	200@10	Small
Ru NPs		74@10	105	50@10	2025, 21, 2506131

ORR

Catalysts	Electrolyte	Half-wave potential (V)	Stability @CV (cycles)	Reference

View Article Online
DOI: 10.1039/D6SC02823C

$L1_2$-Pt_3Co/Ti-a-NPC	0.1 M $HClO_4$	0.936	3 mV decay@3000	Adv. Funct. Mater.
$L1_2$-Pt_3Co/a-NPC		0.926	5 mV decay@3000	2024, 34, 2406347
$L1_0$-Cr-PtFe/C	0.1 M $HClO_4$	0.952	2.9% decay@30000	J. Am. Chem. Soc.
$L1_0$-PtFe/C		~0.92	20.2% decay@30000	2024, 146, 2033−2042
FePc/Eu_2O_3	0.1 M KOH	0.939	9 mV decay@20000	Adv. Funct. Mater.
FePc		0.906	22 mV decay@20000	2025, 35, 2425138
Mn SAs/Fe_3C NPs@NPC	0.1 M KOH	0.88	No decay@10000	Nano Res.
Fe_3C NPs@NPC		~0.8	N/A	2022, 15, 7976–7985
FeRu-DACs	0.5 M H_2SO_4	~0.83	15 mV decay@20000	Angew. Chem. Int. Ed.
Fe-N-C		~0.79	N/A	2025, 64, e202508141
Fe-N_3S/SNC	1 M KOH	0.924	1 mV decay@5000	Adv. Energy Mater.
Fe-N_4/NC		0.9	N/A	2026, 0, e71096

CO_2RR

Catalysts	Electrolyte	E (V)	Faraday efficiency	Reference
CuO-C_{60}	1 M KOH	-1.6	61%@C_{2+} products	Adv. Energy Mater.
CuO			32%@C_{2+} products	2023, 13, 2204346
G-Cu_xO-2 h	1 M KOH+ 0.5 M $KHCO_3$	-0.8	81%@formic acid	Appl. Catal., B
Cu_xO-2 h			29.7%@formic acid	2019, 259, 118044
CuCeO-O_v	1 M KOH + 0.1 M $KHCO_3$	-1.3	51.7%@C_2H_4	Appl. Catal., B
CuO-O_v			33.5%@C_2H_4	2026, 395, 126871
C_{60}/Cu(OH)F	0.1 M $KHCO_3$	-1.5	76.9%@C_{2+} products	Chem. Commun.
Cu(OH)F			45.3%@C_{2+} products	2025, 61, 1681–1684
c-Cu_2O–C_{60}	1 M KOH+ 0.1 M $KHCO_3$	-1.2	60.4%@C_{2+} products	ACS Nano
c-Cu_2O		-1.4	46.6%@C_{2+} products	2025, 19, 41658−41668

NRR/NO_3RR

Catalysts	Electrolyte	Faraday efficiency @E (V)	NH_3 yield @E (V)	Reference
STRs	0.1 M HCl	24.56%@-0.3	21.54 μg h^{-1} mg^{-1}@-0.3	Adv. Sci.
Te NWs		8.77%@-0.3	6.15 μg h^{-1} mg^{-1}@-0.3	2019, 6, 1901627
Ag^0-$CuAgO_x$	0.1 M KOH + 0.01 M KNO_3	91.5%@-0.6	1920 μg h^{-1} cm^{-2}@-0.6	Adv. Energy Mater.
Cu nanosheet		~25%@-0.6	~400 μg h^{-1} cm^{-2}@-0.6	2025, 15, 2405534
Cu_2O-In_{SA}	0.5 M Na_2SO_4 + 0.1 M KNO_3	99.36%@-0.8	23.37 mg h^{-1} mg^{-1}@-0.8	Angew. Chem. Int. Ed.
Cu_2O		~80%@-0.8	~15 mg h^{-1} mg^{-1}@-0.8	2026, 65, e20730
$Fe(OH)_2$/Fe@CNTs	1 M KOH + 0.1 M KNO_3	95.1%@-0.4	0.67 mmol h^{-1} cm^{-2}@-0.4	Adv. Funct. Mater.
$Fe(OH)_2$@CNTs		~75%@-0.4	~0.45 mmol h^{-1} cm^{-2}@-0.4	2025, 35, 2501079
Fe@CNTs		~92%@-0.4	~0.38 mmol h^{-1} cm^{-2}@-0.4	

5.1. OER

Under highly oxidizing conditions, electrocatalysts (e.g., Ru and Co-based materials) often suffer inevitable over-oxidation during OER process, leading to structural degradation and diminished stability.[55,56] However, high-valence metal sites typically exhibit superior catalytic activity due to the more empty d-orbitals that preferably adsorb intermediates.[57] Moreover, the OER process is constrained by the linear scaling relationships among oxygen-contained intermediates, which fundamentally limits further enhancement of the catalytic activity.[58]

In this context, the electron buffer effect has emerged as a pivotal regulatory mechanism to address these issues by modulating

the electronic structure of active sites.[33,39,59–63] Qiao et al. introduced Re dopants into RuO_2 to simultaneously boost OER activity and stability.[59] Leveraging the multivalent nature of Re and its strong metal-oxygen bonding capability, the authors effectively induced dynamic charge transfer at the Ru sites. *In situ* XANES analysis revealed a progressive increase in the oxidation state of Re (from +6.33 to +6.67) during the pre-catalytic process with the increasing potential. As the potential exceeded 1.3 V, the oxidation state of Re decreased from +6.67 to +6.29 due to the electron acceptance from Ru, facilitating the generation of high-valence Ru sties to boost electrocatalytic activity. At even higher overpotential (>1.5 V), the Re sites (from +6.29 to +6.53) donated electrons back to Ru, preventing their over-oxidation and thereby preserving the structural integrity of RuO_2 (Fig. 6a). This reversible electron exchange enabled Re dopants to function as an effective electron reservoir, dynamically activating and stabilizing the Ru sites, and significantly promoting the OER performance of RuO_2 (Fig. 6b). $Re_{0.06}Ru_{0.94}O_2$ showed the overpotential of 190 mV at 10 mA cm^{-2} and maintained 200 h at 10 mA cm^{-2}, outperforming RuO_2 (258 mV and 20 h at 10 mA cm^{-2}). Beyond valence state regulation, the electron buffer effect can also optimize the adsorption behaviors of OER intermediates by tuning the electronic structure of active sites. Chen et al. employed a 2D C_{60} network to precisely modulate the electronic structure of the Ir nanoclusters (Ir NCs/C_{60}NET).[32] Ir NCs/C_{60}NET exhibited the overpotential of 237 mV at 10 mA cm^{-2} and great stability of 600 h at 10 mA cm^{-2}. Owing to the unique electron buffer effect of C_{60}NET, the Ir NCs/C_{60}NET showed a higher anodic peak ($Ir^{3+} \rightarrow Ir^{4+}$) compared to Ir NCs/graphene, indicating the enhanced resistance to oxidation of Ir^{3+} (Fig. 6c). Besides, the buffering by C_{60}NET significantly suppressed the increase in reduction current for Ir NCs/C_{60}NET, demonstrating that electrons from Ir NCs were partially captured by C_{60}NET rather than being fully transferred to the electrode. Bader charge analysis further confirmed the strong electron-withdrawing and electron-donating ability of C_{60}NET, which dynamically modulate the electron density of the Ir NCs (Fig. 6d). Besides, the *in situ* Ir L_3-edge XANES quantitatively analyzed the electron buffer strength of C_{60}NET. The Ir NCs/C_{60}NET showed the lower increase rate [$\partial\mu$(E)/$\partial\eta$] of 0.6 for the intensities of the white line peaks relative to the overpotential than that of Ir NCs/graphene (0.84) from the open-circuit voltage (OCV) to 1.65 V vs. RHE, indicating the oxidation state of Ir in Ir NCs/C_{60}NET can be retarded with the electron buffer effect of C_{60}NET. More importantly, during the OER process, the electron buffer effect of C_{60}NET increased the electron density on Ir nanoclusters while decreasing it on reaction intermediates, thereby promoting the formation of *OOH. This electronic redistribution narrowed the free energy difference between ΔG_{*OOH} and ΔG_{*OH}, breaking the conventional linear scaling relationship ($\Delta G_{*OOH} - \Delta G_{*OH}$ = 3.2 ± 0.2 eV) for single-site catalyst and consequently reducing the energy barrier of rate-determining step (RDS) (Fig. 6e). Besides, a P-Ce SAs@CoO catalyst with Ce(4f)–O(2p)–Co(3d) gradient orbital coupling was designed to optimize the adsorption energies of oxygen-containing intermediates.[38] The introduction of Ce into CoO induced surface charge redistribution. The Ce acts as an electron donor with a higher charge than Co, which alleviates Co self-oxidation. Moreover, the RDS of OER switch from *O to *OOH in CoO to *OH to *O in P-Ce SAs@CoO with the decreased energy barrier of RDS, and the scaling relation ($\Delta G_{*OOH} - \Delta G_{*OH}$) of P-Ce SAs@CoO reduce from 3.3 to 3.25 eV, indicating the enhanced OER performance. These findings underscore the potential of the electron buffer effect in rationally modulating the thermodynamics of surface electrocatalytic reactions.

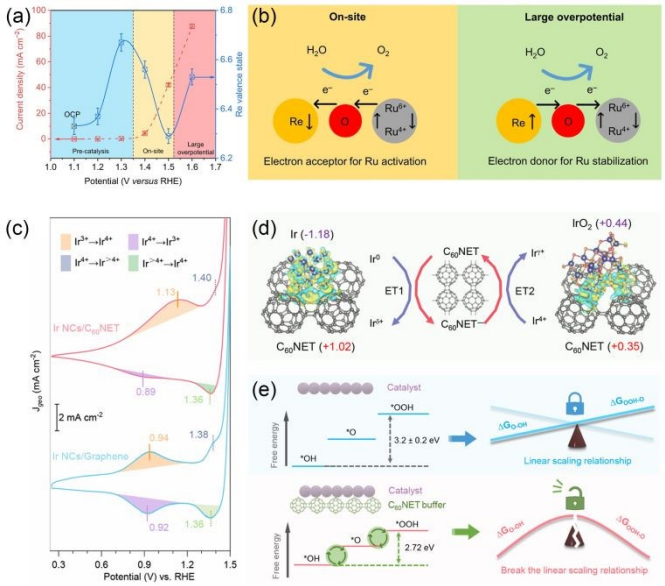

Fig. 6 (a) The change of Re valence state and OER current density as a function of applied potential. (b) Schematic illustration of dynamic electron transfer between Re and Ru sites. Reproduced with permission.[59] Copyright 2023, Springer Nature. (c) The cyclic voltammetry (CV) curves of Ir NCs/C_{60}NET and Ir NCs/graphene. (d) The Bader charge values for Ir-C_{60}NET and IrO_2-C_{60}NET systems. (e) Schematic illustration of conventional and C_{60}NET-buffered correlations among OER intermediates. Reproduced with permission.[32] Copyright 2025, American Chemical Society.

5.2. HER

The HER proceeds through a two-electron transfer pathway comprising the Volmer step followed by either Heyrovsky or Tafel step.[64] While optimizing the adsorption strength of *H intermediate at active sites to align with the Sabatier principle has been widely demonstrated to boost HER activity, the critical initial steps of H_2O adsorption and activation remain frequently overlooked in mechanistic studies.[65,66] Given that the electron density of active sites significantly influences the adsorption and activation of H_2O, the introduction of the electronic buffer effect holds promise for enhancing these processes.[49,67] For instance, Ma et al. constructed a Mo nanolayer as electron buffer between Pt and Mo_2C (Pt_1@Mo_L/Mo_2C) via a carburization method under a reductive atmosphere.[68] Bader charge analysis revealed a strong electron interaction between Pt site and Mo_2C (0.76 |e|), as well as with the interfacial Mo (0.49 |e|). Upon inserting a single Mo atomic layer between Pt and Mo_2C, the Bader charge on Pt decreases to 0.35 |e|, and further dropped to 0.04 |e| when the Mo nanolayer was increased to three atomic layers (Fig. 7a). The Mo nanolayer effectively weakened the electron interaction between Pt and Mo_2C substrate by mitigating the electron withdrawal from the Mo_2C matrix. Moreover, the electron buffer effect primarily originated from the second and third Mo layers, which remained nearly charge-neutral (Fig. 7b). Density functional theory (DFT) calculation

indicated that the Mo nanolayer not only improved H_2O accumulation and adsorption, but also promoted H_2O activation and dissociation into *H and *OH. Besides, the electron buffer effect rendered Pt sites in a near-zero valence state with a free-atom-like *d* state, facilitating the adsorption/desorption of dissociated *H on Pt sites. As a result, the synergistic interaction between Mo nanolayer and Pt sites enabled $Pt_1@Mo_L/Mo_2C$ with an optimal HER performance (Fig. 7c). Pt_1-Mo_L-Mo_2C showed the HER overpotential of 12 mV at 10 mA cm^{-2}, which is lower than that of Pt_1-Mo_2C (47 mV). In addition to water activation, maintaining active sites in a desirable valence state is equally crucial for precise modulation of the adsorption affinity for key reaction intermediates during HER. For instance, Wang et al. introduced Cu dopant as an electron buffer to regulate the electronic structure of RuO_2 supported on titanium felt (RCO/TF) during HER.[69] Owing to the multivalence nature of Cu (+2/+1/0) under HER potential, the dynamically adaptive electron buffer effect facilitates the generation of active Ru^0/Ru^{4+} surface while suppressing the excessive reduction of Ru species. Post-HER characterization confirmed that the Ru^{4+}/Ru^0 ratio in RCO/TF remained nearly unchanged, whereas RuO_2/TF showed an obvious increase in the proportion of Ru^0 (Fig. 7d). The resulting partial oxygen-deficient Ru^0-rich surface on the Cu-doped RuO_2 showed a more favorable hydrogen adsorption energy than single Ru and RuO_2, delivering the enhanced HER activity with the overpotential of 17 mV at 10 mA cm^{-2}. Therefore, the electronic buffer effect exhibits multiple functions in HER electrocatalysis, though its underlying mechanisms warrants further systematic investigation.

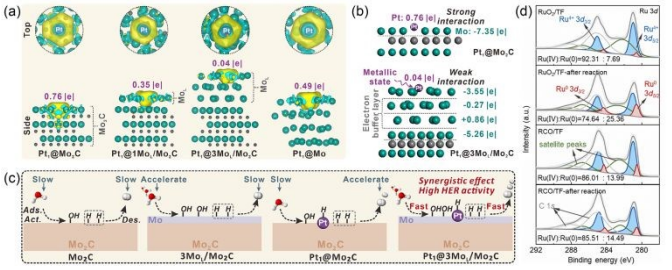

Fig. 7 (a) Charge density distribution and Bader charge of the Pt_1 site in different structures. (b) Bader charge of the Mo nanolayer in $Pt_1@Mo_2C$ and $Pt_1@3Mo_L/Mo_2C$. (c) Schematic illustration of HER process on different surface structures. Reproduced with permission.[68] Copyright 2025, Wiley-VCH. (d) The Ru 3d XPS spectra of RuO_2/TF, RuO_2/TF-after reaction, RCO/TF, and RCO/TF-after reaction. Reproduced with permission.[69] Copyright 2025, Royal Society of Chemistry.

5.3. ORR

As a multi-electron transfer process that proceeds in the reverse direction of the OER, the ORR also presents a fundamental challenge in achieving the balanced adsorption of oxygen-contained intermediates at active sites.[70,71] Although Pt-based materials remain benchmark ORR catalysts, the integration of an electron buffer component offers a promising strategy to not only reduce material cost but also finely tune the d-band center of Pt sites, thereby optimizing the adsorption behavior of key reaction intermediates.[28,31,72,73] Cheng et al. designed a Ti single atom-modified nitrogen-doped porous carbon (Ti-a-NPC) to balance the O_2 activation and *OH desorption on ultra-small $L1_2$-Pt_3Co nanoparticles.[31] Functioning as an electron buffer with electron-withdrawing ability, the Ti atoms trapped electrons and modulated the electron transfer from $L1_2$-Pt_3Co to the N atoms, thus regulating the local electron density at the Pt sites (Fig. 8a–c). The resulting charge rearrangement on Ti atoms formed an electron channel bridging the support and $L1_2$-Pt_3Co (Fig. 8d). This interaction significantly shifted the *d*-band center of Pt sites, thereby tuning the adsorption energy for oxygen-contained intermediates. The optimized O bonding strength of $L1_2$-Pt_3Co/Ti-a-NPC that buffered by Ti single atoms promoted O_2 activation and switched the RDS to the *OH removal, thereby enhancing the intrinsic ORR activity (Fig. 8e). $L1_2$-Pt_3Co/Ti-a-NPC showed the higher half-wave potential of 0.936 V, compared to $L1_2$-Pt_3Co/a-NPC (0.926 V). In addition to Pt-based materials, other metal-based materials integrated with electron buffer components can also effectively regulate the adsorption behavior of reaction intermediates, thereby enhancing electrocatalytic performance.[74–78] Luo et al. designed a Fe single atom catalyst (Fe-N_3S/SNC) with a broken D_{4h} symmetric structure by substituting a N atom in the Fe–N_4 moiety with a S atom, resulting in a Fe-N_3S coordination.[74] The S atom, with lower electronegativity than N, acts as an electron buffer that dynamically maintains a stable electron filling in the e_g orbital of Fe during ORR. Compared with symmetric Fe–N_4 site, the Fe–N_3S site preserves an e_g filling value close to 1 throughout the ORR. This stability originates from the electron buffer capability of S, which can reversibly accept or donate electrons to compensate for the charge density variation on Fe. Consequently, the energy barrier for electron transfer between t_{2g} and e_g orbitals is lowered, facilitating the formation of *OOH and the desorption of *OH. Thus, Fe-N_3S/SNC catalyst achieves an outstanding half-wave potential of 0.924 V vs. RHE in alkaline OER. Moreover, the electron buffer effect can also be extended to dual-atom configuration to regulate the behavior of reaction intermediates for ORR. Xiang et al. implanted isovalent Ru ions into the secondary coordination structure of an Fe–N_4 site, forming FeRu dual-atom catalysts (FeRu-DACs).[75] The Ru center with highly similar d-orbital characteristics to Fe serve as an electron buffer site that dynamically neutralizes the electronic polarization induced by the adsorption of oxygen-containing intermediates. Therefore, the Ru lowers the Fe d-band center by only 0.27 eV, shifting the RDS from *OH desorption to *OOH to *O conversion and reducing the energy barrier. Besides, FeRu-DACs achieve a peak power density of 1.73 W cm^{-2} in H_2-O_2 fuel cells and retain over 97 % of Fe sites after prolonged stability tests, which is a 22-fold improvement over Fe-N-C. The stabilization of FeRu-DACs during ORR process is attributed to the reversible electron transfer between Fe and Ru sites. Notably, the electron buffer effect contributes significantly to both catalytic activity and stability, as further demonstrated in rare-earth-based systems. The f-band in rare-earth materials can serve as an electron buffer to preserve covalency by compensating electron loss, thereby boosting the electrocatalytic performance of active centers.[79,80] Fu et al. constructed an *f-p-d* gradient orbital coupling configuration by integrating Fe phthalocyanine with Eu_2O_3 (FePc/Eu_2O_3) on carbon nanotubes to achieve an efficient and stable ORR electrocatalysis.[80] Owing to the intrinsically higher energy level of Eu 4*f* orbitals relative to the lower Hubbard band (LHB) in Fe–O*, the adsorbed oxygen intermediates preferentially extracted electrons from the Eu *f*-band rather than the Fe *d*-orbitals (Fig. 8f). This electron buffer effect from

Eu *f*-band with electron-donating ability maintained the covalency and high-spin *d*-orbital occupancy of Fe–N_4 sites, significantly achieving the enhanced ORR stability. Furthermore, the *f-p-d* gradient orbital coupling facilitated the O–O bond cleavage in *OOH and shifted the RDS of FePc/Eu_2O_3 from *OOH→*O to *O→*OH, thereby boosting the ORR activity (Fig. 8g). Compared with FePc (0.906 V and 20000 cycles with 22 mV degradation), FePc/Eu_2O_3 exhibited the higher half-waver potential of 0.939 V and greater stability of 20000 cycles with 9 mV degradation. In summary, the electron buffer effect serves as a versatile electronic regulation strategy that concurrently enhances both the activity and stability of ORR electrocatalysts.

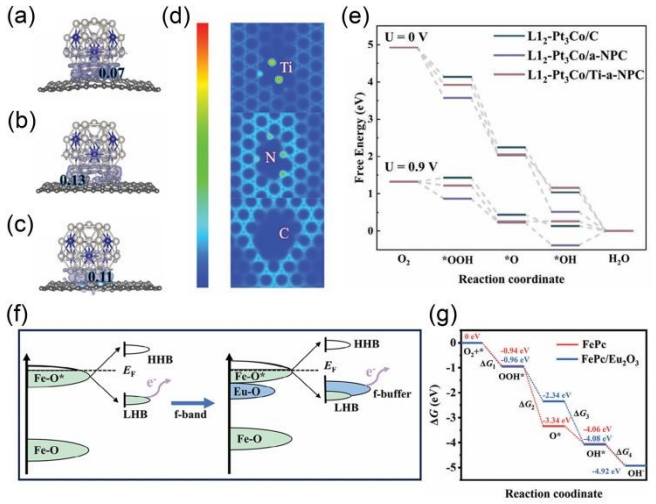

Fig. 8 The charge density difference distribution of L1$_2$-Pt_3Co supported on (a) C, (b) a-NPC, and (c) Ti-a-NPC. (d) Electron localization function diagram and (e) free energy diagram of L1$_2$-Pt_3Co/Ti-a-NPC, L1$_2$-Pt_3Co/a-NPC, and L1$_2$-Pt_3Co/C. Reproduced with permission.[31] Copyright 2024, Wiley-VCH. (f) Schematic illustrations of the proposed f-p-d gradient orbital coupling effect on ORR activity and stability. (g) Free energy diagram of FePc and FePc/Eu_2O_3. Reproduced with permission.[80] Copyright 2025, Wiley-VCH.

5.4. CO_2RR

The electrochemical CO_2RR faces challenges in product selectivity, primarily due to the diverse CO_2 adsorption configurations and complex reaction pathway, along with severe competition from the HER.[81–86] The HER-inert Cu-based materials serve as the most promising candidate for steering the product distribution of CO_2RR.[87] However, Cu^+ sites are prone to the reduction to Cu^0 during CO_2RR process, particularly at high negative potentials. As an effective strategy for regulating the valence states, the electron buffer effect has demonstrated significant applicability in Cu-based systems.[88,89] Yan et al. introduced an electron buffer effect by decorating Cu_xO on graphene oxide (G-Cu_xO).[88] During the electrocatalytic process, Cu^{2+} species act as a sacrificial agent, continuously replenishing Cu^+ active sites from the bulk to the surface of Cu_xO, thereby enhancing catalytic stability. Meanwhile, the stabilized Cu^+ sites effectively weaken the adsorption strength of *COOH intermediates, leading to improved selectivity toward HCOOH. The synthesized G-Cu_xO-2 h showed higher Faraday efficiency (FE) (81%) at -0.8 V toward HCOOH than Cu_xO-2 h (29.7%). Currently, the conversion of CO_2 into high-value multicarbon (C_{2+}) products holds immense economic and environmental interest, yet it faces a key challenge due to the difficulty in facilitating C–C coupling. It has been reported that the coupling between *CHO and *CO intermediates is thermodynamically and kinetically favorable.[90] The Cu-based materials with Cu^0-Cu^+ active sites are considered promising for facilitating the generation of *CHO intermediates, which are crucial for the subsequent formation of C_{2+} products.[91,92] Zhang et al. synthesized a CuO-C_{60} composite with *in situ* formed Cu^0-Cu^+ dual active sites after electroreduction.[89] The charge density difference analysis confirmed that the generation and stabilization of Cu^+ sites originated from the electron transfer from Cu^0 sites to C_{60}, which possesses a strong electron-withdrawing ability (Fig. 9a). In contrast to the maintained valence state distribution of Cu in the CuO-C_{60} structure, the Cu species in pure CuO were completely reduced to Cu^0 within 10 min of electrolysis (Fig. 9b and c). Moreover, *in situ* attenuated total reflection FTIR (ATR-FTIR) verified the presence of *CHO and coupled *CO-CHO intermediates on CuO-C_{60}, indicating the preferential coupling between *CO and *CHO over *CO dimerization at the Cu^0-Cu^+ dual sites (Fig. 9d). Compared with CuO (32%), CuO-C_{60} showed higher FE of 61% for C_{2+} products. In addition, the FE ratio of C_{2+} products to CO for CuO-C_{60} was also higher than that for CuO, especially at high reduction potentials, further demonstrating the crucial role of the electron buffer effect in promoting C–C coupling (Fig. 9e). Yuan et al. developed a cubic Cu_2O–C_{60} catalyst for CO_2RR.[93] The C_{60} molecules act as an electron buffer, dynamically accepting and donating electrons during CO_2RR, thereby preventing over-reduction of Cu^+ to Cu^0. This electron buffer effect maintains abundant Cu^+/Cu^0 grain boundaries on the surface of catalyst. The *in situ* Raman spectra of c-Cu_2O–C_{60} showed the both presence of Raman bands of the atop-bound (2085–2125 cm^{-1}) and bridge-bound (1785–1876 cm^{-1}) *CO species, which are essential for efficient C–C coupling, while only weak *CO_{atop} adsorption was observed on the c-Cu_2O surface. Hence, C_{60} acts as a molecular electron reservoir that preserves the active Cu^+/Cu^0 interface, promotes *CO dimerization, and dramatically enhances both C_{2+} selectivity and long-term durability. The c-Cu_2O–C_{60} catalyst achieved FEs for C_{2+} product of 60.4% in the H-cell and 65.6% in the flow cell, and maintaining stable operation for 100 h at –1.2 V vs. RHE without obvious activity loss. Moreover, Wu et al. synthesized a Ce-doped CuO catalyst enriched with oxygen vacancies (CuCeO-O_v).[94] In the synthesized gradient orbital coupling O_v-[Ce 4f-O 2p-Cu 3d] unit, the Ce 4f orbitals serve as electron buffer, while the O_v act as an electron supply station, enhancing Cu–O covalency and stabilizing the $Cu^{\delta+}$ (1<δ<2) state during CO_2RR. The *in situ* FTIR spectra was used to identify key reaction intermediates during CO_2RR. Compared to pristine CuO-O_v, CuCeO-O_v exhibited significantly stronger infrared bands at ~1557 cm^{-1} (*COCHO of the C–C coupling), ~1772 cm^{-1} (*CHO), and 1735 cm^{-1} (*C_2H_4), indicating that the electron buffer effect from Ce and O_v promoted the formation and stabilization of *CHO and facilitated its coupling with *CO to generate *COCHO. Moreover, in a CuO catalyst with oxygen vacancies, the Bader charge of the C atom in adsorbed *CHO is 1.65 |e|. After Ce doping, this value increases to 1.82 |e|, which facilitates electron transfer to the adsorbed *CHO and strengthens the Cu–C bond. Besides, the energy barrier for coupling *CO and *CHO to generate *COCHO of CuCeO-O_v is lowered than that of CuO-O_v, which is consistent with the higher FE of C_2H_4 (51.7% at –1.3 V vs.

RHE). In summary, the electron buffer effect plays an important role in the modulation of metal valence state and the adsorption behavior of key intermediates, thereby governing CO_2RR product selectivity.

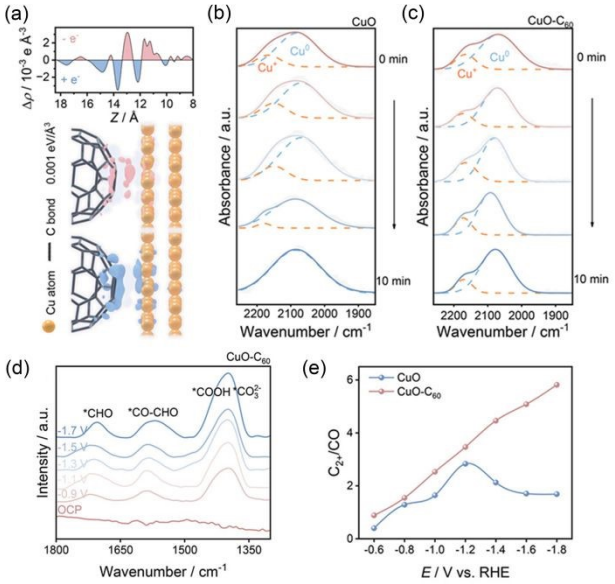

Fig. 9 (a) The charge density difference and planar-averaged electron density difference for C_{60}-Cu systems. *In situ* ATR-FTIR spectra of (b) CuO and (c) CuO-C_{60} at different times. (d) *In situ* ATR-FTIR spectra of CuO-C_{60} at different potentials. (e) The FE ratios of C_{2+} products to CO of CuO and CuO-C_{60} at different potentials. Reproduced with permission.[89] Copyright 2023, Wiley-VCH.

5.5. Ammonia Synthesis

The ammonia production from electrochemical NRR presents a sustainable and efficient route that circumvents the energy-intensive conditions and high-pressure H_2 requirements of the conventional Haber-Bosch method.[95,96] However, the extreme inertness of the N_2 molecule severely limits NRR activity, making efficient N_2 adsorption and activation a critical challenge.[97–99] TeO_2, which exhibits inert HER activity, demonstrates considerable N_2 activation capability due to its exposed lone-pair electrons that facilitate N–N bond elongation (Fig. 10a). Nevertheless, O ligands in TeO_2 cannot buffer the oxidation state variation of Te during NRR. To address this limitation, Li et al. introduced Se into TeO_2 to enhance the hybridization between Te 5p and O 2p orbitals, increasing the DOS near Fermi level (Fig. 10b).[100] The incorporation of Se promoted efficient charge transfer from Te sites to N_2, significantly reducing the adsorption energy of N_2 (Fig. 10c), leading to the higher FE (24.56%) and NH_3 yield (21.54 g h^{-1} mg^{-1}) at –0.3 V. Moreover, the resulting electron-donating SeO ligands near Te sites served as electron reservoirs to effectively buffer the oxidation state of Te, which is critical for π-backdonation interaction between Te sites and N_2. This electronic modulation also shifted the RDS from the protonation of *NNH to that of *N_2, lowing the energy barrier to 0.98 eV (Fig. 10d). Given the persistent inefficiency in cleaving the highly stable triple bond of N_2, the NO_3RR has emerged as a thermodynamically more favorable alternative for ammonia production, owing to the high solubility and lower activation barrier of nitrate.[101–103] In one representative study, Li et al. constructed heterovalent $Fe(OH)_2$/Fe pair sites on carbon nanotubes ($Fe(OH)_2$/Fe@CNTs) to drive efficient NO_3RR.[104] The d-band center for $Fe(OH)_2$/Fe (1.104 eV) show an upward shift toward the Fermi level compared to Fe (0.622 eV) alone, and a downward shift compared to $Fe(OH)_2$ (3.478 eV) alone, tuning adsorption energies of N-containing intermediates. The $Fe(OH)_2$/Fe structure provided both a sufficient proton source and moderate *NO_3 adsorption affinity, facilitating continuous hydrogenation steps during NO_3RR. Compared to single Fe and $Fe(OH)_2$, the $Fe(OH)_2$/Fe configuration delivered the lowest energy barrier for the RDS, indicating the superior nitrate-to-ammonia efficiency (Fig. 10e). $Fe(OH)_2$/Fe@CNTs showed higher FE (95.1%) and NH_3 yield (0.67 mmol h^{-1} cm^{-2}) at –0.4 V by comparing with $Fe(OH)_2$@CNTs (almost 75% and 0.45 mmol h^{-1} cm^{-2}) and Fe@CNTs (almost 92% and 0.38 mmol h^{-1} cm^{-2}). Crucially, the electron transfer between Fe and $Fe(OH)_2$ induced the electron buffer effect that dynamically stabilized the $Fe(OH)_2$/Fe sites when exposed in air and during electroreduction, thereby maintaining both catalytic activity and structural integrity throughout the NO_3RR process. Besides, Wang et al. developed a heterostructured catalyst composed of metallic Ag clusters embedded in oxidized $CuAgO_x$ nanosheets (Ag^0-$CuAgO_x$).[105] The Ag^0 acts as an electron buffer, dynamically accepting electrons from Cu^+ to generate electron-deficient Cu sites, thus modulating the Cu d-band center (from –2.82 eV to –2.54 eV relative to the Fermi level) with the optimized adsorption/activation energy barriers of *NO_2 and *NO intermediates, which steering the reaction selectivity toward NH_3 rather than nitrite or H_2. As shown in the *in situ* FTIR spectra, the peak that assigned to *NO_2 emerges at –0.4 V vs. RHE on Ag^0-$CuAgO_x$, while Cu nanosheet showed the *NO_2 peak at a more negative potential of –0.8 V vs. RHE, demonstrating the enhanced kinetics of nitrate-to-nitrite conversion on Ag^0-$CuAgO_x$. Moreover, compared to the Cu nanosheet, as the potential becomes more negative, a much wider redshift for the band position of *NO_2 and *NO on Ag^0-$CuAgO_x$ can be observed, indicating the higher stark tuning rate and stronger electric field of Ag^0-$CuAgO_x$ with the electron-deficient Cu sites, which can strengthen the activation of *NO_2 and *NO and facilitate the subsequent hydrogenation to NH_3. In addition, DFT results showed that Cu_2O-Ag model possess a lower energy barrier of the RDS (*NO to *NOH) than that of Cu and Cu_2O. Hence, Ag^0-$CuAgO_x$ exhibited a high FE of 91.5% and a NH_3 yield rate of 1920 μg h^{-1} cm^{-2} at –0.6 V vs. RHE. These studies collectively demonstrate that introducing electron buffer components can effectively stabilize the oxidation state of active metals, lower the energy barrier of RDS, and enhance the selectivity and stability toward valuable ammonia production. Although the electron buffer effect has demonstrated preliminary potential in stabilizing metal sites and modulating the adsorption behavior of N-contained intermediates, its precise regulatory mechanisms governing complex reaction pathways and product selectivity in electrocatalytic ammonia synthesis require further exploration.

View Article Online
DOI: 10.1039/D6SC02837C

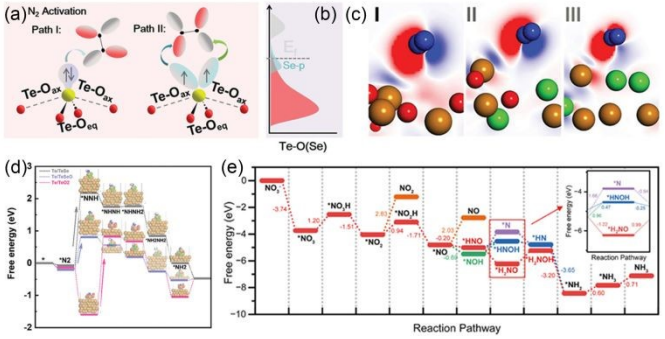

Fig. 10 (a) The N_2 activation on TeO_2 through backbonding interactions. (b) Schematic band diagrams of TeO_2 after introduction of Se. (c) Charge density difference of N_2-adsorbed TeO_2, TeSeO, and TeSe. (d) Schematic illustration of free energy diagram for Te/TeSe, Te/TeSeO, and Te/TeO_2. Reproduced with permission.[100] Copyright 2019, Wiley-VCH. (e) Free energy diagram of NO_3RR on $Fe(OH)_2$/Fe via different pathways. Reproduced with permission.[104] Copyright 2025, Wiley-VCH.

6. Summary and Outlook

In summary, precise modulation of the electronic structure of active sites through the introduction of an electron buffer effect has emerged as a pivotal strategy for enhancing electrocatalytic performance. This approach offers considerable potential for boosting activity, improving stability, and steering reaction pathways, thereby offering a novel avenue for overcoming the performance limitations of conventional electrocatalysts. Current research on the electronic buffer effect is undergoing a paradigm evolution, progressing from phenomenological description to mechanistic understanding, and further advancing toward rational design. Although this review has summarized key progress in this field, there are still several serious challenges that guide future research directions (Fig. 11).

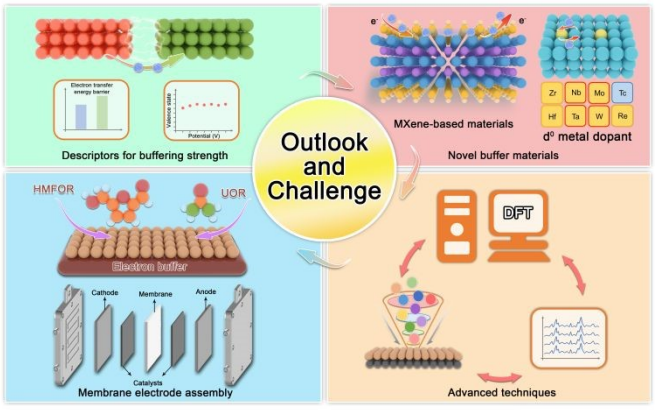

Fig. 11 Schematic illustration of outlook and challenges for electron buffer effect.

6.1. Establishing evaluation criteria for buffering strength

To quantitatively assess electron buffering capability, a multi-dimensional framework that integrates complementary theoretical and experimental descriptors is essential. Theoretically, a key metric is the interfacial electron transfer energy barrier, which quantifies the thermodynamic driving force for electron transfer between the buffer component and the active sites. A lower interfacial electron transfer energy barrier corresponds to a more facile and reversible buffering process in the catalyst. Concurrently, the projected Density of States (pDOS) analysis of catalyst with and without the buffer component can reveal the extent of electronic modulation. The shifts in d-band center and changes in electron occupancy near the Fermi level serve as intrinsic descriptors directly correlated to adsorption energetics. Experimentally, the multi-potential step stability test can determine the operational potential window of the buffer component by monitoring activity retention (e.g., current or potential decay) under progressively oxidizing or reducing conditions. A wider stable potential window indicates greater applicability. Furthermore, *in situ* X-ray absorption spectroscopy (XAS) can track the valence state of the active metal as a function of applied potential (E). The d(valence state)/dE reflects the potential-dependent sensitivity of the metal center. Therefore, a smaller d(valence state)/dE over the relevant potential range signifies stronger buffering strength, as it indicates effective suppression of over-oxidation or over-reduction. Thus, a robust evaluation of buffering strength necessitates the integrated application of these complementary descriptors, which bridge theoretical insight with experimental validation to enable systematic comparison across different buffer systems.

6.2. Rational design of novel buffer materials

Based on first-principles calculations and high-throughput screening, it is feasible to identify novel buffer materials featuring broader potential windows and higher electron affinity. For instance, MXene ($M_{n+1}X_nT_x$, where M is a transition metal, X is C and/or N, and T is surface functional groups) represents an innovative class of catalyst supports for electrocatalysis. Its two-dimensional layered architecture, coupled with high electrical conductivity, intrinsic hydrophilicity, tunable interlayer spacing, and abundant terminal functional groups (e.g., -O, -OH, -F), render it a highly attractive platform. The conductive backbone of transition metal carbides/nitrides ensures efficient charge transport, while the terminal functional groups can serve as electron donors or acceptors. This dual functionality allows for flexible modulation of the electronic structure of the supported active components, making MXene as a promising candidate for advanced electron buffer material. Furthermore, introducing multiple variable-valence metals as dopants into the active component not only simplifies the synthetic process, but also effectively induces the electron buffer effect by leveraging their multivalent characteristics. Among these, high-valent d^0 metal ions (e.g., W^{6+}, Mo^{6+}, Nb^{5+}) are the promising candidates due to their fully empty d-orbitals, which allow the high-valent d^0 metal ions to function as the electron reservoirs. During the initial stage of oxidation reactions, these empty d-orbitals accept electrons and promote the formation of high-valent active centers. Subsequently, by donating electrons back, high-valent d^0 metal ions can mitigate over-oxidation of the active sites during prolonged operation. Thus, engineering with high-valent d^0 metal dopants directly addresses the interfacial instability issue in conventional supported catalysts, while simultaneously enhancing the overall buffering capacity.

6.3. Advanced *in situ* characterization and simulation techniques

Current investigations on the electron buffer effect in catalysts predominantly rely on the static electronic structure analysis conducted before and after reactions. The *in situ* characterization techniques and dynamic theoretical simulations based on first-principles calculations will be crucial for advancing fundamental research on the electron buffer effect. By employing *in situ* XANES, the dynamic valence state evolution of active sites in response to the changes of potential or time can be tracked during catalytic processes, which can be used to quantify the buffering strength, allowing for the direct assessment of the electron buffer effect. In addition, *in situ* EXAFS can provide insights into the dynamic evolution of the coordination structure of active sites, reflecting changes in local electronic structure and geometric configuration around metal atoms. The *in situ* XPS allows for the quantitative tracking of valence state distributions in both metal-based buffer materials and active sites, thereby directly revealing the dynamic electron redistribution processes at their interface. Furthermore, *in situ* infrared and Raman spectroscopy can analyze the evolution of reaction intermediates on the surface of catalyst. A systematic correlation of these findings with the valence state evolution of active sites enables a direct investigation into the mechanistic role of the electron buffer effect in steering the reaction pathway. Furthermore, constant-potential density functional theory (DFT) combined with *ab initio* molecular dynamics (AIMD) simulations enables the accurate modeling of dynamic interfacial evolution between the buffer component and active sites under an applied electric field. Analyses of the density of states (DOS), band structure, and differential charge density can directly reveal the electron transfer pathways between buffer component and active sites. Additionally, comparing the adsorption energies of key intermediates with and without the buffer component can elucidate how the electron buffer effect modulates the reaction pathway.

6.4. Expansion and integration strategies for the electrocatalytic application

During electrocatalysis, the local pH near the electrode surface can deviate substantially from the bulk value, particularly under high current densities where rapid proton consumption or generation occurs. Such local pH changes may significantly affect the redox behavior of metal‑based electron buffer components. Most of works focus on bulk electrolyte pH effects on catalytic activity or product selectivity rather than on the reversible electron transfer dynamics of the buffer component itself. The future investigations on electron buffer effect should also focus on the microenvironment changes on the surface of electrode, which can guide the design of robust electrocatalysts for practical high-current-density operation. The electron buffer effect has been extensively applied in the fields of OER, HER, and ORR. Future research should emphasize on its underexplored role in CO_2RR and NRR/NO_3RR, where its influence on reaction pathways and product selectivity remains unclear. A mechanistic understanding in these systems is urgently needed. Extending this concept to organic oxidation reactions, particularly the urea oxidation reaction (UOR), and 5-hydroxymethylfurfural oxidation reaction (HMFOR) that proceed via *in situ* formation of high-valence metal oxyhydroxide species (e.g., NiOOH, CoOOH), represents a promising avenue for further research.[106–108] The buffer component in these organic oxidation reactions can act as an electron acceptor, facilitating the oxidation of metal centers and lowering the kinetic barrier for generating active high‑valence species. Moreover, as reported by Du et al., NiOOH can undergo over-oxidation to form OER-favored species (e.g., $NiO(OH)_2$ and NiO_2), particularly under conditions of high applied potential or when the concentration of organic molecules adsorbed on the catalyst surface is insufficient.[109] Acting as a reversible electron donor, the buffer component can supply electrons to the metal center when its valence state increases excessively. This mechanism ensures that the catalyst remains in its optimal oxidation state for efficient organic molecule activation. Besides, through fine modulation of electron density of active site, the buffer component tunes the adsorption/desorption behavior of key intermediates, balances surface coverages of organic molecules and OH^-, and promotes selective bond activation to direct the reaction toward desired products. For example, favoring C–N bond cleavage over N–H bond cleavage in UOR for higher Faraday efficiency of NO_x^- products. Hence, an effective electron buffer component for these organic oxidation reactions should meet two key criteria: intrinsic OER inertness to suppress the competition of OER, and the efficient electron storage/release capacity that can dynamically regulate the valence states of active sites. Based on the abovementioned potential for regulation in catalytic reactions, translating the electron buffer effect into practical applications still requires overcoming a series of challenges, necessitating a focused research pathway that moves from scalable material synthesis to practical device validation. To address scalable manufacturing, future work should develop facile synthesis routes for incorporating variable-valence metals into the bulk phase of active components. This approach inherently bypasses the need for complex interfacial control, which is often difficult to scale up. Besides, to validate long-term durability, device-level integration must be assessed by fabricating membrane electrode assemblies and performing accelerated stress tests under operating conditions (e.g., potential cycling). Finally, system-level optimization requires integrating the electron buffer effect with electrode architectures designed for efficient mass and charge transport, supported by economic analysis to assess practical feasibility. This roadmap aims to translate the concept of electron buffer effect from precisely defined materials into robust and scalable electrochemical devices.

Overcoming the existing bottlenecks hinges on the deep integration of multi-scale theoretical simulations, artificial intelligence, and advanced *in situ* characterization techniques. By synergistically employing these tools, the accurate prediction and rational design of the electron buffer effect will be ultimately achieved. Through such mechanistic insights and material innovations, the electron buffer effect is expected to drive rapid advancement in electrocatalysis and plays a significant role in energy conversion, chemical production and environmental remediation.

Author contributions

All of the authors contributed to the literature search, writing and editing of this review.

Conflicts of interest

There are no conflicts to declare.

Data availability

No primary research results, software or code have been included and no new data were generated or analysed as part of this review.

Acknowledgements

This work was financially supported by the National Natural Science Foundation of China (22571275, 21975223, 52473034), Natural Science Foundation of Zhejiang Province (LZ22B030002, LQN26B030005), Jinhua Major Project (2024-3-001), Jinhua Key Project (2026-3-098), and Open Research Fund of Key Laboratory of the Ministry of Education for Advanced Catalysis Materials and Zhejiang Key Laboratory for Reactive Chemistry on Solid Surfaces, Zhejiang Normal University (YS136X23002).

References

1 S. Chu and A. Majumdar, *Nature*, 2012, **488,** 294–303.
2 N. S. Lewis, *Science*, 2016, **351**, aad1920.
3 K. Kawashima, R. A. Marquez, L. A. Smith, R. R. Vaidyula, O. A. Carrasco-Jaim, Z. Wang, Y. J. Son, C. Cao and C. B. Mullins, *Chem. Rev.*, 2023, **123**, 12795–13208.
4 M. B. Ross, P. De Luna, Y. Li, C. T. Dinh, D. Kim, P. Yang and E. H. Sargent, *Nat. Catal.*, 2019, **2**, 648–658.
5 H. Ding, H. Liu, W. Chu, C. Wu and Y. Xie, *Chem. Rev.*, 2021, **121**, 13174–13212.
6 M. F. Lagadec and A. Grimaud, *Nat. Mater.*, 2020, **19**, 1140–1150.
7 L. Chong, G. Gao, J. Wen, H. Li, H. Xu, Z. Green, J. D. Sugar, A. J. Kropf, W. Xu, X. Lin, H. Xu, L. Wang and D. Liu, *Science*, 2023, **380**, 609–616.
8 T. Wang, X. Cao and L. Jiao, *Angew. Chem., Int. Ed.*, 2022, **61**, e202213328.
9 L. Quan, H. Jiang, G. Mei, Y. Sun and B. You, *Chem. Rev.*, 2024, **124**, 3694–3812.
10 L. Yan, P. Li, Q. Zhu, A. Kumar, K. Sun, S. Tian and X. Sun, *Chem*, 2023, **9**, 280–342.
11 H. Wang, X. Kang and B. Han, *Chem. Soc. Rev.*, 2025, **54**, 10156–10244.
12 Y. Ren, C. Yu, X. Tan, H. Huang, Q. Wei and J. Qiu, *Energy Environ. Sci.*, 2021, **14**, 1176–1193.
13 Y. Xiong, Y. Wang, J. Zhou, F. Liu, F. Hao and Z. Fan, *Adv. Mater.*, 2024, **36**, 2304021.
14 H. Chem, X. Liang, Y. Liu, X. Ai, T. Asefa and X. Zou, *Adv. Mater.*, 2020, **32**, 2002435.
15 C. Hu, R. Paul, Q. Dai and L. Dai, *Chem. Soc. Rev.*, 2021, **50**, 11785–11843.
16 R. W. Zhang, J. L. Sun, Y. Z. Chen, Q. Shen, C. Ding, S. Zhang and J. Zhang, *Coord. Chem. Rev.*, 2025, **543**, 216958.
17 H. Wang, L. Chen, H. Pang, S. Kaskel and Q. Xu, *Chem. Soc. Rev.*, 2020, **49**, 1414–1448.
18 S. J. Tauster, *Acc. Chem. Res.*, 1987, **20**, 389–394.
19 T. Pu, W. Zhang and M. Zhu, *Angew. Chem., Int. Ed.*, 2023, **62**, e202212278.
20 P. Yin, Q. Yan and H. Liang, *Angew. Chem., Int. Ed.*, 2023, **62**, e202302819.
21 S. Lyu, C. Guo, J. Wang, Z. Li, B. Yang, L. Lei, L. Wang, J. Xiao, T. Zhang and Y. Hou, *Nat. Commun.*, 2022, **13**, 6171.
22 J. Zheng, L. Huang, C. Cui, Z. Chen, X. Liu, X. Duan, X. Cao, T. Yang, H. Zhu, K. Shi, P. Du, S. Ying, C. Zhu, Y. Yao, G. Guo, Y. Yuan, S. Xie and L. Zheng, *Science*, 2022, **376**, 288–292.
23 Y. Zhang, X. Peng, H. Tian, B. Yang, Z. Chen, J. Li, T. Zhang, M. Zhang, X. Liang, Z. Yu, Y. Zhou, L. Zheng, X. Wang, J. Zheng, Y. Tang, C. T. Au, L. Jiang and S. Xie, *Nat. Chem.*, 2024, **16**, 1781–1787.
24 M. Zhang, Y. Luo, X. Peng, S. Zhang, L. Zhang, C. Xu, Y. Zhou, L. Zheng, J. Ni, X. Wang, L. Jiang and J. Li, *Adv. Funct. Mater.*, 2025, **35**, 2415651.
25 Y. Zi, C. Zhang, J. Zhao, Y. Cheng, J. Yuan and J. Hu, *Small*, 2024, **20**, 2406657.
26 Z. Li, J. Yi, Y. Tang, Z. Zhang, C. Li, R. Bao and J. Wang, *Energy Environ. Sci.*, 2025, **18**, 7188–7202.
27 Z. Liu, H. Liu, T. Xue, K. Zhou, C. Li, Y. Shen, X. Su, Z. Wu, H. Li, H. Li and C. Li, *Nano Lett.*, 2024, **24**, 10899–10907.
28 X. Liu, Y. Wang, J. Liang, S. Li, S. Zhang, D. Su, Z. Cai, Y. Huang, L. Elbaz and Q. Li, *J. Am. Chem. Soc.*, 2024, **146**, 2033–2042.
29 F. Qian, D. Cao, S. Chen, Y. Yuan, K. Chen, P. J. Chimtali, H. Liu, W. Jiang, B. Sheng, L. Yi, J. Huang, C. Hu, H. Lei, X. Wu, Z. Wen, Q. Chen and L. Song, *Nat. Commun.*, 2025, **16**, 6894.
30 Z. Zhao, Y. Zhao, W. Wang, X. Xin, Y. Jiao, A. D. Abell, C. S. Law and A. Santos, *Adv. Sci.*, 2026, **13**, e14558.
31 Z. Wang, W. Wu, H. Jiang, S. Chen, R. Chen, Y. Zhu, Y. Xiao, H. Lv, J. Zhong and N. Cheng, *Adv. Funct. Mater.*, 2024, **34**, 2406347.
32 X. Chen, H. Ma, X. Wang, H. Jin, Y. Wu, S. Wang, Y. Xiao, R. Jiang, Y. Da, L. Fan, Y. Sun, S. Xi, Y. Lum, Q. He, H. Li, D. Liu, S. Yang and W. Chen, *J. Am. Chem. Soc.*, 2025, **147**, 20600–20611.
33 L. Deng, S. Huang, Z. Lin, Y. Zhang, C. Zhang, Y. Hao, S. Liu, C. Kuo, H. Chen, J. Peng, J. Wang and S. Peng, *Adv. Mater.*, 2023, **35**, 2305939.
34 Y. Wang, J. Wang, J. Xu, X. Qu, L. Lin, L. Zhao, Q. Liu, Y. Wei, X. Li, Q. Ma, J. Zhang, W. Fan, B. Wu, X. Kong, J. Huang, Y. Wang, Y. Ye, Y. Feng and F. Zhang, *Angew. Chem., Int. Ed.*, 2025, **64**, e202503608.
35 Z. Dong, C. Zhou, W. Chen, F. Lin, H. Luo, Z. Sun, Q. Huang, R. Zeng, Y. Tan, Z. Xiao, H. Huang, K. Wang, M. Luo, F. Lv and S. Guo, *Adv. Funct. Mater.*, 2024, **34**, 2400809.
36 J. Shang, X. Zhang, Y. Che, X. Qin, Y. Zhang, J. Zhang, B. Li, C. Yang, Y. Jiang, X. Lin and Q. Liu, *J. Mater. Chem. A*, 2025, **13**, 23998–24004.
37 X. Zou, X. Zhao, B. Pang, H. Ma, K. Zeng, S. Zhi and H. Guo, *Adv. Mater.*, 2024, **36**, 2412954.
38 M. Li, X. Wang, K. Liu, H. Sun, D. Sun, K. Huang, Y. Tang, W. Xing, H. Li and G. Fu, *Adv. Mater.*, 2023, **35**, 2302462.
39 X. Wang, Z. Li, H. Jang, C. Chen, S. Liu, L. Wang, M. Kim, J. Cho, Q. Qin and X. Liu, *Adv. Energy Mater.*, 2025, **15**, 2403388.
40 W. Gou, Z. Xia, X. Tian, Q. Xue, F. Ye, S. Dai, M. Zhang, R. Si, Y. Zou, Y. Ma, J. Ho and Y. Qu, *Nano Energy*, 2022, **104**, 107960.
41 H. Yue, S. Huo, X. Wang, M. Wang, H. Sun, Y. Chen, Y. Dai, M. Liu and J. Zou, *Mater. Today*, 2025, **89**, 44–56.
42 D. Kim, S. Jo, J. I. Jeon, J. I. Sohn and J. Hong, *Energy Environ. Mater.*, 2025, **0**, e70136.
43 Y. Zhi, Z. Li, Y. Tang, J. Peng, Z. Zhang, C. Li, R. Bao, G. Chen, J. Yi, J. Chen, J. Wang and J. Wang, *Nano Energy*, 2025, **134**, 110565.
44 J. Chen, M. Aliasgar, F. B. Zamudio, T. Zhang, Y. Zhao, X. Lian, L. Wen, H. Yang, W. Sun, S. M. Kozlov, W. Chen and L. Wang, *Nat. Commun.*, 2023, **14**, 1711.
45 Y. H. Choi, J. Lee, A. Parija, J. S. Cho, S. V. Verkhoturov, M. Al-Hashimi, L. Fang and S. Banerjee, *ACS Catal.*, 2016, **6**, 6246–6254.
46 R. Gao, Q. Dai, F. Du, D. Yan and L. Dai, *J. Am. Chem. Soc.*, 2019, **141**, 11658–11666.

47 L. Hou, X. Cui, B. Guan, S. Wang, R. Li, Y. Liu, D. Zhu and J. Zheng, *Nature*, 2022, **606**, 507–510.
48 E. Meirzadeh, A. M. Evans, M. Rezaee, M. Milich, C. J. Dionne, T. P. Darlington, S. Bao, A. K. Bartholomew, T. Handa, D. J. Rizzo, R. A. Wiscons, M. Reza, A. Zangiabadi, N. Fardian-Melamed, A. C. Crowther, P. J. Schuck, D. N. Basov, X. Zhu, A. Giri, P. E. Hopkins, P. Kim, M. L. Steigerwald, J. Yang, C. Nuckolls and X. Roy, *Nature*, 2023, **613**, 71–76.
49 X. Wang, X. Chen, R. Lv, H. Ma, Y. Yao, H. Jin, S. Qiao, Y. Sun, D. Liu, L. Song, P. Du, W. Chen, Y. Lu and S. Yang, *Small*, 2025, **21**, 2506131.
50 Q. Tang, L. Wang, S. Zhang, P. Xue, Y. Zhang, H. Li and D. Zhu, *J. Mater. Chem. A*, 2025, **13**, 5229–5237.
51 Y. Li, T. Xu, Q. Huang, L. Zhu, Y. Yan, P. Peng and F. Li, *ACS Catal.*, 2023, **13**, 7597–7605.
52 Q. Li, X. Wang, Z. Xie, X. Peng, L. Guo, X. Yu, X. Yang, Z. Lu, X. Zhang and L. Li, *Appl. Catal., B*, 2022, **350**, 121020.
53 Y. Lu, B. Li, N. Xu, Z. Zhou, Y. Xiao, Y. Jiang, T. Li, S. Hu, Y. Gong and Y. Cao, *Nat. Commun.*, 2023, **14**, 6965.
54 Y. Hao, S. Hung, C. Tian, L. Wang, Y. Chen, S. Zhao, K. Peng, C. Zhang, Y. Zhang, C. Kuo, H. Chen and S. Peng, *Angew. Chem., Int. Ed.*, 2024, **63**, e202402018.
55 L. Wang, S. Hung, S. Zhao, Y. Wang, S. Bi, S. Li, J. Ma, C. Zhang, Y. Zhang, L. Li, T. Chen, H. Chen, F. Hu, Y. Wu and S. Peng, *Nat. Commun.*, 2025, **16**, 3502.
56 J. Huang, C. N. Borca, T. Huthwelker, N. S. Yuezbasi, D. Baster, M. El Kazzi, C. W. Schneider, T. J. Schmidt and E. Fabbri, *Nat. Commun.*, 2024, **15**, 3067.
57 H. Wang, T. Zhai, Y. Wu, T. Zhou, B. Zhou, C. Shang and Z. Guo, *Adv. Sci.*, 2023, **10**, 2301706.
58 Z. Huang, J. Song, S. Dou, X. Li, J. Wang and X. Wang, *Matter*, 2019, **1**, 1494–1518.
59 H. Jin, X. Liu, P. An, C. Tang, H. Yu, Q. Zhang, H. Peng, L. Gu, Y. Zheng, T. Song, K. Davey, U. Paik, J. Dong and S. Qiao, *Nat. Commun.*, 2023, **14**, 354.
60 L. Jiang, J. Chen, Y. Zhou, J. Liu, F. Liu, Z. Zhang, J. Qin, Y. Lai and J. Li, *ACS Appl. Mater. Interfaces*, 2025, **17**, 47047–47056.
61 Y. Wang, K. Wei, Y. Song, A. A. Obisanya, H. Li, J. Wang, H. Li and F. Gao, *Chem. Eng. J.*, 2024, **497**, 154724.
62 X. Yang, S. Li, Y. Zhang, F. Qiu, Y. Sun, W. Ning, Q. Tao, W. Li and S. Miao, *J. Mater. Chem. A*, 2024, **12**, 17574–17585.
63 H. Jin, S. Choi, G. J. Bang, T. Kwon, H. S. Kim, S. J. Lee, Y. Hong, D. W. Lee, H. S. Park, H. Baik, Y. Jung, S. J. Yoo and K. Lee, *Energy Environ. Sci.*, 2022, **15**, 1119–1130.
64 M. N. Hossain, L. Zhang, R. Neagu and S. Sun, *Chem. Soc. Rev.*, 2025, **54**, 3323–3386.
65 C. Xu, H. Yu, H. Huang, S. Li, Y. Cao, W. Peng, Y. Li, H. Ke, S. Xu, H. Mo, C. Wu, H. Wang, Y. Zhang, X. Li and W. Chen, *Angew. Chem., Int. Ed.*, 2025, **64**, e202504667.
66 M. Jiang, J. Xu, Q. Zhou, Y. Chen, P. Munroe, L. Li, Z. Xie, Y. Wu and S. Peng, *Angew. Chem., Int. Ed.*, 2025, **64**, e202510259.
67 M. Maji, S. Dutta, R. Jena, A. Dey, T. K. Maji, S. K. Pati and S. Bhattacharyya, *Angew. Chem., Int. Ed.*, 2024, **63**, e202403697.
68 L. Xu, Y. Xu, B. Xia, B. Guo, K. M. Kamal, B. Likozar, X. Li, F. Dong, S. Li and Y. Ma, *Adv. Mater.*, 2025, **37**, 2502989.
69 X. Wang, T. Liu, J. Wang, B. Xia, Y. Wang, Z. Li, Z. Zhang and F. Wang, *J. Mater. Chem. A*, 2025, **13**, 14964–14971.
70 A. Kulkarni, S. Siahrostami, A. Patel and J. K. Norskov, *Chem. Rev.*, 2018, **118**, 2302–2312.
71 Y. Pan, M. Li, W. Mi, M. Wang, J. Li, Y. Zhao, X. Ma, B. Wang, W. Zhu, Z. Cui, H. Yin and Y. Liu, *Nano Res.*, 2022, **15**, 7976–7985.
72 M. Zhou, H.-L. Wang and S. Guo, *Chem. Soc. Rev.*, 2016, **45**, 1273–1307.
73 X. Mou, Z. Zhang, Z. Zhao, B. Liu, X. Wang, C. Yang, L. Shen, Y. Zhang, L. Zhao, W. Qu and Z. Wang, *Int. J. Hydrogen Energy*, 2025, **182**, 151698.
74 Y. Xie, Y. Feng, S. Pan, Q. Xu, Z. Yang, J. Zhang, X. Fu and F. Luo, *Adv. Energy Mater.*, 2026, **0**, e71096. View Article Online DOI: 10.1039/D6SC02823C
75 H. Yu, C. Li, Y. Lei and Z. Xiang, *Angew. Chem., Int. Ed.*, 2025, **64**, e202508141.
76 N. Li, K. Guo, S. Lu, L. Bao, Z. Yu and X. Lu, *Chem. Commun.*, 2024, **60**, 11964–11967.
77 R. Jin, C. Guo, Y. Si, Y. Liu, L. Teng, F. Fu, Y. Jian, X. Dong and T. G. Cherkasova, *J. Mater. Chem. A*, 2026, **14**, 14499–14512.
78 Y. Liu, Z. Wang, S. Cao, F. Liu, Q. Tan, Y. Chen and W. Wang, *J. Mater. Chem. A*, 2026, **14**, 20394–20404.
79 M. Li, X. Wang, K. Liu, Z. Zhu, H. Guo, M. Li, H. Du, D. Sun, H. Li, K. Huang, Y. Tang and G. Fu, *Adv. Energy Mater.*, 2023, **13**, 2301162.
80 R. Cheng, X. He, M. Jiang, X. Shao, W. Tang, B. Ran, H. Li and C. Fu, *Adv. Funct. Mater.*, 2025, **35**, 2425138.
81 T. Yan, X. Chen, L. Kumari, J. Lin, M. Li, Q. Fan, H. Chi, T. J. Meyer, S. Zhang and X. Ma, *Chem. Rev.*, 2023, **123**, 10530–10583.
82 J. He, J. Hua, Z. Wang, Y. Xia, C. Shao and K. Dai, *Small*, 2025, **21**, 2503852.
83 Y. Xiao, J. Chen, G. Chen, X. Geng, L. Fan, Y. Ding, M. Wang, H. Jin, S. Xi, X. Chen and W. Chen, *Small*, 2026, **22**, e14087.
84 W. Zhang, Y. Wang, L. Cui, M. Wang and K. Yu, *J. Mater. Chem. A*, 2026, **14**, 17316–17327.
85 S. Wen, J. Wen, M. Zhao, Z. Huang, L. Gao and Z. He, *J. Environ. Chem. Eng.*, 2026, **14**, 123311.
86 X. Xiong, X. Wu, Y. Cheng, D. Yu, X. Xu, Y. Cheng, F. Wu and X. Wei, *Chem. Commun.*, 2025, **61**, 1681–1684.
87 X. He, L. Lin, X. Li, M. Zhu, Q. Zhang, S. Xie, B. Mei, F. Sun, Z. Jiang, J. Cheng and Y. Wang, *Nat. Commun.*, 2024, **15**, 9923.
88 W. Ni, C. Li, X. Zang, M. Xu, S. Huo, M. Liu, Z. Yang and Y. Yan, *Appl. Catal., B*, 2019, **259**, 118044.
89 B. Zhao, F. Chen, C. Cheng, L. Li, C. Liu and B. Zhang, *Adv. Energy Mater.*, 2023, **13**, 2204346.
90 X. Zhi, A. Vasileff, Y. Zheng, Y. Jiao and S. Qiao, *Energy Environ. Sci.*, 2021, **14**, 3912–3930.
91 H. Xiao, W. A. Goddard III, T. Cheng and Y. Liu, *Proc. Natl. Acad. Sci. U. S. A.*, 2017, **114**, 6685–6688.
92 E. Bertheussen, A. Verdaguer-Casadevall, D. Ravasio, J. H. Montoya, D. B. Trimarco, C. Roy, S. Meier, J. Wendland, J. K. Norskov, I. E. L. Stephens and I. Chorkendorff, *Angew. Chem., Int. Ed.*, 2016, **55**, 1450–1454.
93 N. Chen, X. Deng, Z. Chen, P. Du, X. Liu, J. Liu, B. Hong, R. Qin, J. Zheng, J. Li, S. Xie and Y. Yuan, *ACS Nano*, 2025, **19**, 41658–41668.
94 J. Wang, J. Li, F. Wang, X. Zhang, S. Liu, S. Niu, L. Chen and X. Wu, *Appl. Catal., B*, 2026, **395**, 126871.
95 Y. Pang, C. Su, G. Jia, L. Xu and Z. Shao, *Chem. Soc. Rev.*, 2021, **50**, 12744–12787.
96 L. Jiang, X. Zhi, X. Bai and Y. Jiao, *J. Am. Chem. Soc.*, 2025, **147**, 16935–16947.
97 T. Zhang, Z. Che, Y. Song, R. Yao, J. Li, Y. Sun and G. Liu, *Angew. Chem., Int. Ed.*, 2025, **64**, e202514028.
98 H. Cai, J. Wang, Y. Guo and Q. Pan, *Appl. Surf. Sci.*, 2026, **720**, 165232.
99 C. He, L. Wang and W. Zhang, *Appl. Surf. Sci.*, 2026, **726**, 165867.
100 G. Zhang, H. Xu, Y. Li, C. Xiang, Q. Ji, H. Liu, J. Qu and J. Li, *Adv. Sci.*, 2019, **6**, 1901627.
101 Z. Kou, D. Shi, B. Yang, Z. Li, Q. Zhang, J. Lu, T. Zhang, L. Lei, Y. Li, L. Dai and Y. Hou, *Chem. Soc. Rev.*, 2025, **54**, 10796–10844.
102 H. Zhang, K. Fang, J. Yang, H. Chen, J. Ning, H. Wang and Y. Hu, *Coord. Chem. Rev.*, 2024, **506**, 215723.
103 G. Li, X. Wang, H. Pang and H. Ma, *Adv. Sci.*, 2026, **13**, e21317.
104 R. Xia, W. Wang, Y. Zhou, Q. Guan, Y. Liu and W. Li, *Adv. Funct. Mater.*, 2025, **35**, 2501079.

View Article Online
DOI: 10.1039/D6SC02823C

105 H. Huang, Y. Zhang, W. Chen, J. Chen, X. Zou, J. Lv, X. Chen, Z. Shen, Z. Ge, L. Guo, Y. Yao and Y. Wang, *Adv. Energy Mater.*, 2025, **15**, 2405534.
106 J. Li, C. Yin, S. Wang, B. Zhang and L. Feng, *Chem. Sci.*, 2024, **15**, 13659–13667.
107 C. Yin, F. Yang, S. Wang and L. Feng, *Adv. Energy Mater.*, 2025, **15**, e04064.
108 C. Yin, F. Yang, T. Liu, S. Wang and L. Feng, *Adv. Energy Mater.*, 2026, **16**, e70876.
109 R. Luo, Y. Li, L. Xing, R. Zhong, Z. Qian, G. Yin, Y. Wang and L. Du, *Appl. Catal., B*, 2022, **311**, 121357.

View Article Online
DOI: 10.1039/D6SC02823C

Data Availability Statement

No primary research results, software or code have been included and no new data were generated or analysed as part of this review.